



Uit

THE ARCTIC
UNIVERSITY
OF NORWAY

FACULTY OF SCIENCE AND TECHNOLOGY

DEPARTMENT OF ENGINEERING AND SAFETY

Modelling of Marine Icing with Close Range Photogrammetry

Asbjørn Eirik Risholm Haukebø

TEK-3900 Master's Thesis in Technology and safety in the High North

April 2015



Abstract

Installations and vessels operating in the high North in the winter season are likely to be subjected to marine icing. To date there are no sensor technology available to accurately measure the total weight or volume of the ice. Photogrammetry is a universal 3-D measuring technique applied in a wide range of interdisciplinary fields. Agisoft PhotoScan is a photogrammetry software utilizing Structure From Motion (SFM) algorithm to create accurate 3-D mesh models. Scenes involving objects that are not textured, shiny, or transparent are to be avoided. The surface of marine ice has all of these properties. This thesis will investigate if, despite all recommendations not to, and show that the PhotoScan software is capable of creating an accurate 3-D model of a block of salt water ice. The volume of the ice model was calculated to be within less than 1% of the actual volume of the ice, using PhotoScan software.

Preface

This thesis is part of my master's degree at The Arctic University of Norway and researched and written from 2013 to the spring of 2015.

The subject of the thesis is "Modelling of Marine Icing with Close Range Photogrammetry". Working with this thesis has been very challenging, but also rewarding. Since 2007 I've had an increasing interest for GIS applications, and my initial approach to accurately measure the volume of Ice was using ESRI ArcGIS with 3D Analyst. However, my primary research quickly ruled out this option and pointed to Photogrammetry instead. Never having even heard about this technique prior to this work it proved to be a lot to learn, and many problems to solve. Several new Software packages have been installed and tested; some of which was used others evaluated and promptly removed from the workflow. The involvement in an ongoing research program has been motivating, and my former background offshore has given crucial ballast in defining the task at hand. This thesis is a case study and is carried out from the very beginning till the final digital model, with emphasis on the practitioner's point of view.

Acknowledgment

I would like to express my sincere gratitude to my supervisor, Dr. Kåre Edvardsen, for coming up with the idea of this thesis, and his support and guidance in the process has been of great value. Not to mention his knowledge of DIY food, this led me to become a home smoker myself.

My wife for her patience and support, without you I would not have managed to complete this project. Thanks to the game Minecraft that kept my three sons busy while I was writing this thesis.

I also need to acknowledge all the people behind the open source programs MeshLab, CloudCompare and Zoltan Hubai for his DslrDashborad application.

Abbreviations

| | |
|--------|---|
| CMOS | Complementary Metal–Oxide–Semiconductor |
| CPU | Central Processing Unit |
| DIY | Do It Yourself |
| DOF | Depth Of Field |
| DSLR | Digital Single-Lens Reflex |
| EXIF | Exchangeable Image File |
| GCP | Ground Control Points |
| GIS | Geographic Information System |
| GNU | GNU's Not Unix |
| GPU | Graphics Processing Unit |
| ISO | International Organization of Standardization |
| LPG | Liquefied Petroleum Gas |
| NEF | Nikon Electronic Files |
| NGC | Norwegian Coast Guard |
| OpenCL | Open Computing Language |
| OS | Operating System |
| PC | Personal Computer |
| PLY | Polygon File Format |
| PNG | Portable Network Graphics |
| PPM | Parts Per Million |
| RAM | Random Access Memory |
| SDHC | Secure Digital High Capacity |
| SFM | Structure From Motion |
| SW | Software |
| TIFF | Tagged Image File Format |
| UAV | Unmanned Aerial Vehicle |
| VBO | Vertex Buffer Object |

Table of Contents

| | |
|---|------------|
| Abstract | ii |
| Preface | iii |
| Acknowledgment | iv |
| Abbreviations | v |
| Table of Contents | vi |
| 1 Introduction | 1 |
| 1.1 Background | 1 |
| 1.2 Previous work..... | 3 |
| 1.3 Systems for ice detection | 4 |
| 1.3.1 Ice Hawk | 4 |
| 1.3.2 Ice camera | 4 |
| 1.3.3 Icing rate detector | 5 |
| 1.3.4 Microwave Aircraft Icing detection system (MAIDS) | 5 |
| 1.3.5 SMARTboot | 5 |
| 1.3.6 TAMDAR..... | 5 |
| 1.3.7 Vaisala | 6 |
| 1.3.8 Pole ice | 7 |
| 1.4 Scope of the thesis | 8 |
| 1.5 Limitations of this study | 9 |
| 2 Photogrammetry | 11 |
| 2.1 Hardware..... | 14 |
| 3 Method | 15 |
| 3.1 Ice..... | 15 |
| 3.2 Photography | 17 |
| 3.2.1 Capturing Photos | 18 |
| 3.2.2 Pictures file format | 21 |

| | | |
|----------|--|-----------|
| 3.2.3 | DOF and Aperture..... | 22 |
| 3.2.4 | Camera Lens and Blitz..... | 25 |
| 3.3 | Agisoft Software | 26 |
| 3.4 | Agisoft PhotoScan..... | 27 |
| 3.5 | Workflow in PhotoScan | 29 |
| 3.5.1 | Loading photos | 29 |
| 3.5.2 | Align photos | 32 |
| 3.5.3 | Build dense cloud..... | 35 |
| 3.5.4 | Build Mesh | 36 |
| 3.5.5 | Volume calculations | 37 |
| 3.6 | Agisoft Lens..... | 39 |
| 3.7 | Workflow problems that were encountered and solved | 42 |
| 3.7.1 | Reversed z-axis | 42 |
| 3.7.2 | Aligning of bounding box to model..... | 43 |
| 3.7.3 | OpenCL | 43 |
| 3.8 | MeshLab..... | 44 |
| 3.9 | CloudCompare | 46 |
| 4 | Marine ice accretion | 49 |
| 4.1 | Types of ice accretion..... | 49 |
| 4.2 | Conditions for ice accretion | 50 |
| 4.3 | Effects of icing | 51 |
| 5 | Results and discussion | 53 |
| 5.1 | CloudCompare | 53 |
| 5.2 | Ice volume measurements | 55 |
| 5.3 | 3-D Model Construction time | 55 |
| 5.4 | Discussion | 56 |
| 5.5 | Conclusion..... | 59 |

| | | |
|----------|---|-----------|
| 6 | Future work..... | 60 |
| 6.1.1 | Full-scale testing | 60 |
| 6.1.2 | Camera operations in sub-zero temperatures..... | 60 |
| 6.1.3 | Camera positioning | 60 |
| 6.1.4 | File formats and post processing | 61 |
| 6.1.5 | QDslrDashboard PC version..... | 61 |
| 6.1.6 | Active use of Light to identify ice..... | 61 |
| 6.1.7 | Review of Lytro camera | 61 |
| 6.1.8 | Higher quality settings in building dense cloud | 61 |
| 6.1.9 | Automation of workflow..... | 62 |
| 7 | Bibliography | 63 |
| 8 | Table of figures..... | 66 |
| 9 | Appendix | 67 |
| 9.1 | Appendix 1: Exif data..... | 67 |
| 9.2 | Appendix 2: Camera positions for ice | 74 |
| 9.2.1 | Camera positions for ice | 74 |
| 9.2.2 | Camera positions for rubber coated ice | 75 |
| 9.3 | Appendix 3: Phyton script for bounding box alignment..... | 76 |
| 9.4 | Appendix 4: PhotoScan processing reports..... | 77 |

1 Introduction

This chapter will introduce the background, problem description and objectives for the master thesis. The scope and limitations are described at the end of this chapter.

1.1 Background

Ice accretion on offshore structures is a challenge for marine activity areas as the Atlantic Arctic in wintertime. With my background in the mid 1990's from one winter in the Barents Sea on the Norwegian coast guard vessel "NCG Andenes", and a winter season in the Baltic sea as a ship officer on a DNV Class 1A ice going multipurpose LPG- tanker I have first-hand experience of ice accretion on vessels and equipment. I have spent hours on removing ice from deck equipment and the vessel superstructure.

I realized that since then, vessels to date still have to rely on qualified assumptions from ship crew on the volume and weight of ice accretion when operating in waters subjected to icing. In light of the recent increase in oil, gas and tourism activity in the Arctic region, we still lack good tools to determine the actual size and weight of marine icing offshore. Both Zakrewzewski (1987), Ryerson (2009) and Overland(1986) has stated that icing on vessels is a hazard. Following that fishing vessels and smaller boats are more susceptible for icing accretion than larger vessels and permanent installations. The effect of icing varies. From posing a hazard as a slippery surface, blocking safety equipment (lifeboats/rafts and communications), preventing the use of to the severe case where the sheer weight of the ice affects the vessel stability. There have been several incidents where icing caused vessels to capsize and sink (Zakrzewski, 1987) with the loss of both vessel and crew, like the MS Vestfjord in 1989. From the 1970's scientists in the former Soviet Union began measuring ice accretion on medium sized fishing vessels. The purpose was identifying variables and developing algorithms for marine ice accretion (Zakrzewski, 1987). In the following decades, several other countries joined and added their work in this field, and ice accretion models were published; ICEMOD from Norway, RIGICE and "Midgett" from Canada and LEWISE from USA. Researchers from Finland, Japan and the Soviet Union have also contributed in the

field with laboratory testing and model verification. The expected increase in oil and gas activity in the high north has both in the late 80's and now in the last decade lead to an increase in research. The research includes ways of improving ice accretion estimation and means of protecting oil and gas related installations and vessels from the hazards of ice accretion (Ryerson C. C., 2009). Better weather forecasting, winterization measurements and recommendations for vessels, icing forecasts, polar low identifications and so forth. Even with the increase in oil-related activity in the Barents Sea, it is estimated that 50% of all sailings in the area will be fishing vessels. This number has decreased from 58% of all traffic in 2008 (Faglig Forum, 2010). The main difference between fishing and petroleum industry being that fisheries are seasonal, while oil and gas is a year round activity. Reports from the initial studies show that ice measuring was much manual labour, with point-based measurements. Even today many of the technics used are point-based, and the standard delimiter is that they were not designed for the marine environment. If a remote sensing volume based approach works, it can be valuable for the future research in the field, as it could prove both low cost and accurate.

1.2 Previous work

With the digital age, photogrammetry has changed rapidly, and low-cost, high-resolution cameras combined with relatively cheap photogrammetry software has made it possible for amateurs to participate in this field. There are several surveys comparing photogrammetry and laser scanning, as the latter is considered to be more expensive than the former and cost is also a factor to consider when doing precise measurements. In 1999 a study called “The use of close range photogrammetry for studying ice accretion on aerofoil sections” (Collier, 1999) was conducted but without a digital camera and software. The conclusion was that it involved much expertise and manual labour and man-hours. When it comes to ice and ice accretion, there have been done few surveys involving digital photogrammetry. Possibly because it is not recommended to use the software on surfaces that are shiny, translucent and featureless. Laser on similar surfaces (marble) has been investigated (Guy, et al., 2001), with variable results and opposing conclusions.

There have also been studies of ice edge development and similar on glaciers and riverbeds, but without any volume calculations, and using GCP's for size measurement. Several studies published in between 1995-2012 using digital photogrammetry as a method are listing time spent on creating a model as a major drawback of this approach (Collier, 1999) (Samaan, Héno, & Pierrot-Deseilligny, 2013) (Conte, 2014).

1.3 Systems for ice detection

Ryerson gives a good thorough review of the systems available for ice detection, and a brief description follows below. (Ryerson C. C., 2009) It is worth noting that none of the systems reviewed are designed for a marine, offshore environment, and they have limited capabilities in measuring ice thickness. Most of the sensors are point-based, and will not give ice volume data.

1.3.1 Ice Hawk

A system developed to detect ice and snow on surfaces, for aircraft purposes, identifying the need for de-icing and verifying an ice free surface. The system is based on laser light polarization. The presence of ice on the surface will cause the polarization to rotate, illustration 1. The system is capable of detecting ice at a thickness of 0.5 mm.

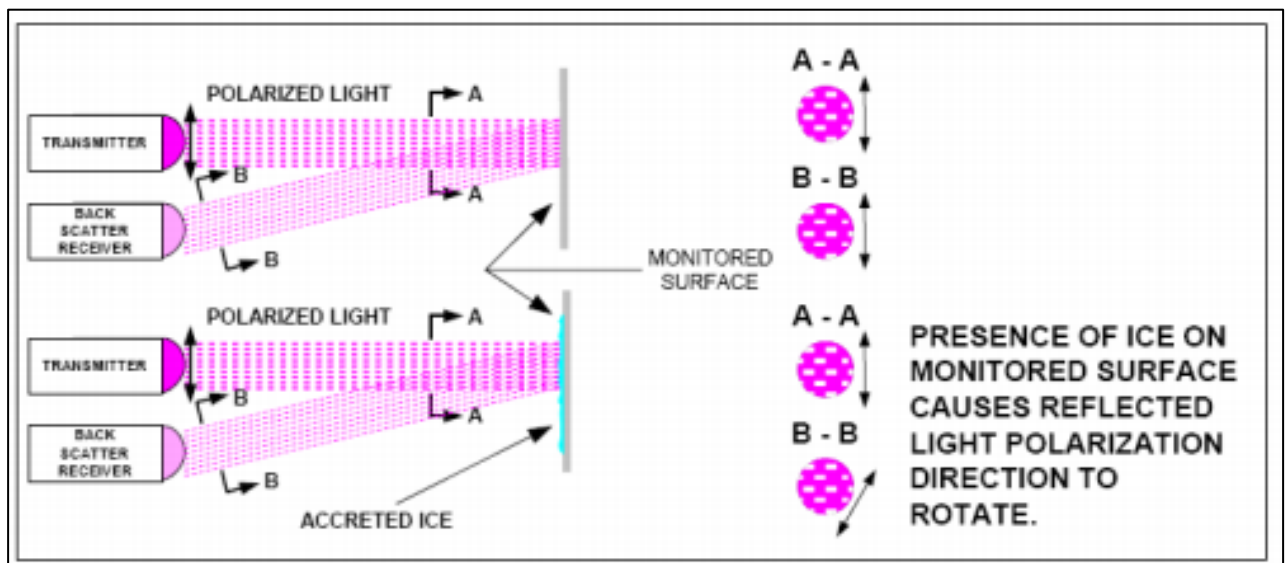


Illustration 1 Rotation of polarized light emitted by sensors show the presence of ice or snow

1.3.2 Ice camera

A system using near infrared wavelengths to detect ice, a strobe emitting infrared light is used in conjunction with the camera that detects the reflections of the energy from the surface. The system is capable to detect ice less than 0.5 mm thick, and can detect icing up to a thickness of 12 mm.

1.3.3 Icing rate detector

The Goodrich Rosemount icing detector senses ice mass on a 25-mm-long by 6-mm-diameter cylindrical probe vibrating at 40 kHz when ice-free. When rime, glaze, or frost accumulates on the probe, the mass and stiffness of the ice causes the frequency to decrease.

1.3.4 Microwave Aircraft Icing detection system (MAIDS)

MAIDS is capable of detecting the presence of ice as thin as 0.025mm up to 6mm. It provides a continuous-wave microwave signal split onto a sensor path and a reference path. Data processing of the two signals computes the magnitude and phase of the sensor signal relative to those of the reference signal. The normalized magnitude and phase response of the system serves as an indication of the thickness of ice and or water.

1.3.5 SMARTboot

SMARTboot is an automatic detection and removal system, based on measuring the impedance between two electrodes. The impedance provides the thickness of the ice. When a predetermined ice thickness is reached, the boots are inflated, and the ice is removed. One system covers an area of 232 cm². This system has not been tested in a saline environment.

1.3.6 TAMDAR

Tropospheric Airborne Meteorological Data Reporting (TAMDAR) is a system for atmospheric monitoring that use infrared emitter and detector to detect the presence of ice. The system is capable of measuring 0.5 mm of ice.

1.3.7 Vaisala

A road and pavement ice detection system. A sensor is built in flush with the surface. This sensor reports road surface condition optical detection, surface conductivity, electrochemical polarizability, surface capacitance for black ice, surface temperature, and ground temperature at a depth of 6 cm. It is capable of measuring ice thickness up to 8mm.

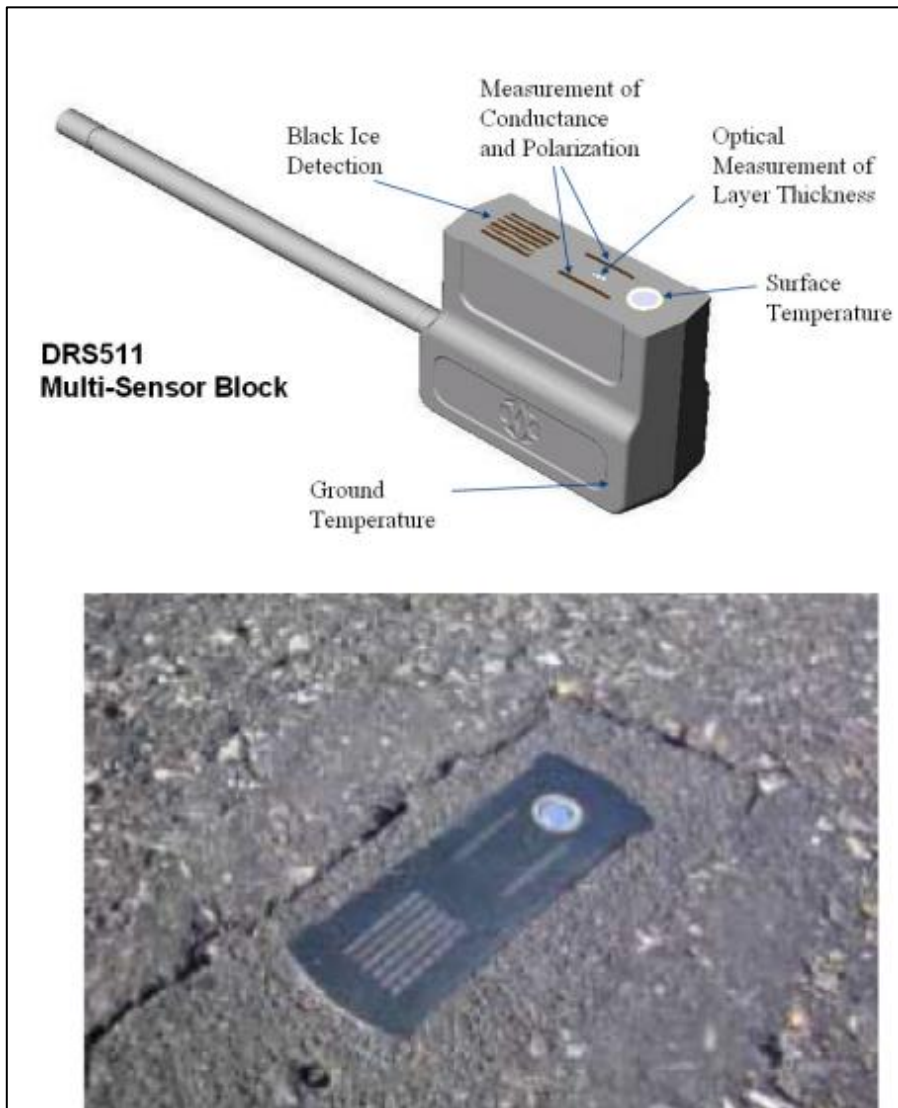


Illustration 2 Vaisala road ice detector

1.3.8 Pole ice

Pole ice was Intended for use along electrical transmission lines. The ice detector was designed for harsh environments. A rod placed on a load cell, and when icing occurs the weight increase on the cell. Mounting the ice pole on a vessel can cause erratic data caused by the ship motion and vibration.

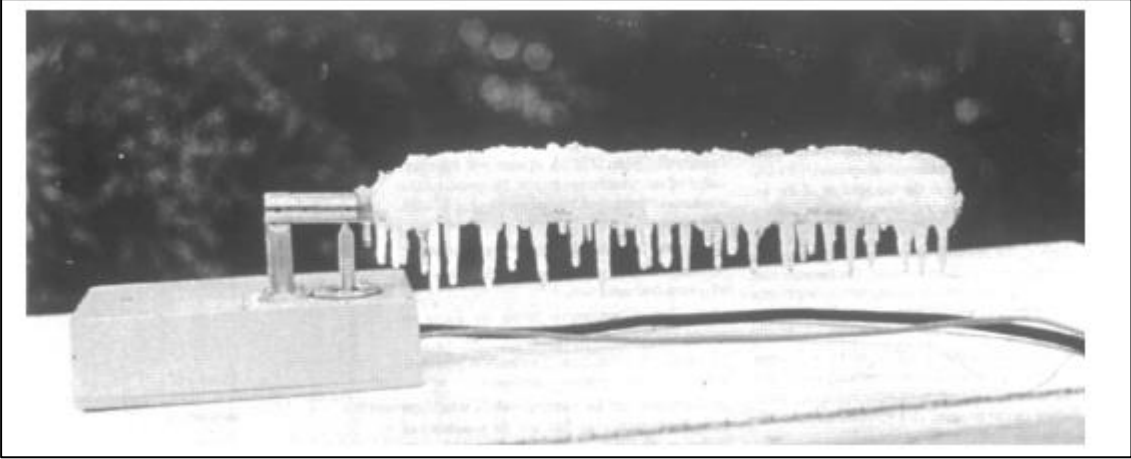


Illustration 3 Pole ice with ice accretion

1.4 Scope of the thesis

In this thesis, the possibility of using low-cost consumer-grade equipment combined with state-of-the-art photogrammetry software to model marine ice is to be investigated. It is further a goal to calculate and verify the volume of the ice model. For the offshore application of an ice measurement system, there is a need for the information to be as close to real-time as possible, to be able to make real-time decisions. This thesis will evaluate the time spent creating the 3-D model and will at all-time try to evaluate the task from an operational point of view. Implying that rather than analysing the algorithms used by the software to achieve the model, the real world implications of adopting the approach will be discussed.

1.5 Limitations of this study

In this thesis, there are aspects that are somehow related to marine ice accretion that will not be discussed mainly because of the timeframe available and the fact that they do not affect the problem being investigated.

- This thesis will not discuss problems related to vessel or installation stability issues caused by marine ice accretion.
- National and international rules and regulations governing the design and operation in polar areas will not be discussed.
- The formulas used for estimating marine icing accretion will not be presented or discussed, as they have no impact on the result of this thesis.
- As a reference for icing and lighting conditions, the Norwegian part of the Barents Sea is used. This mainly because the easy access to the data, and the knowledge of the area.
- The thesis is investigation marine icing in the context of sea spray icing, as this is the most severe and most studied form of marine ice accretion.

2 Photogrammetry

Photogrammetry is a method of image measurement and interpretation in order to derive the shape and location of an object from one or more photographs of that object. Photogrammetry can, in principle, be applied in any situation where the object to be measured can be photographically recorded. The main purpose of a photogrammetric measurement is the three-dimensional reconstruction of an object in digital form (coordinates and geometric elements) or graphical form (images, drawings, maps).

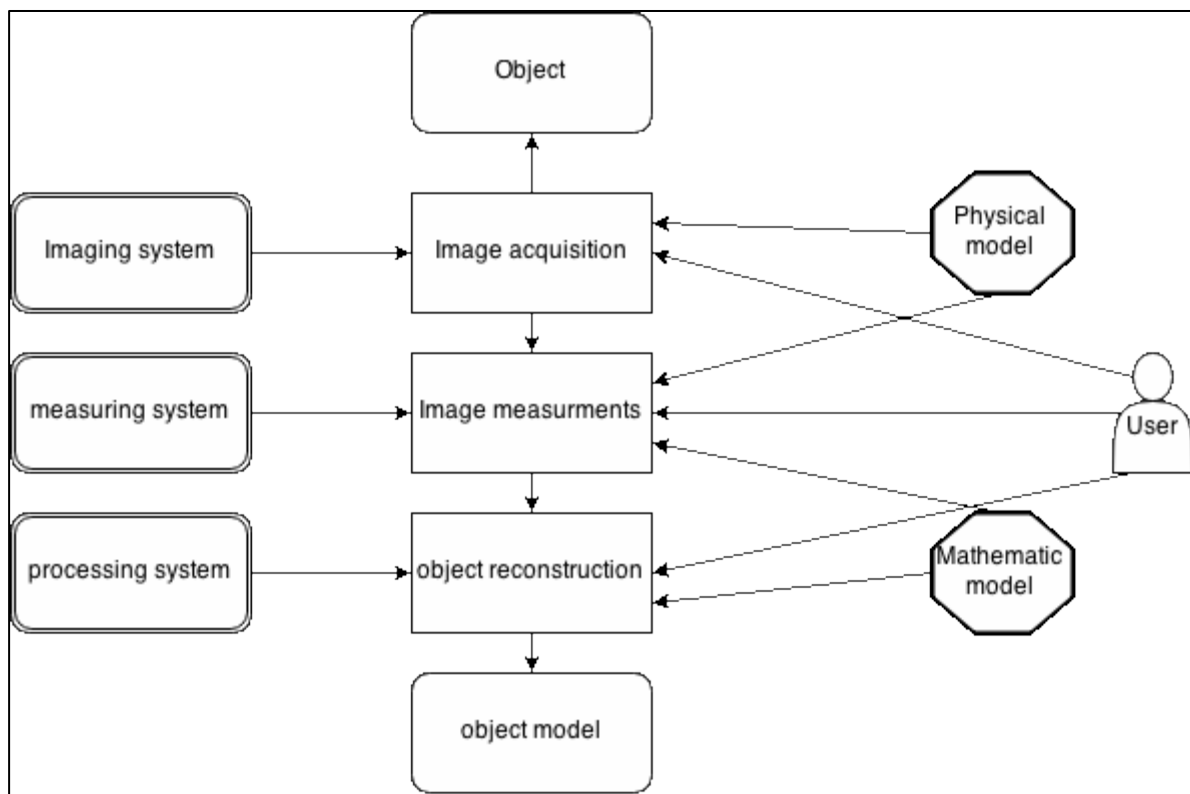


Illustration 4 Photogrammetry model

Close range photogrammetry is not strictly defined, but there is a common understanding that it applies to objects from as small as a trilobite to large objects 200m in size. The accuracy is ranging from 0.1 mm in the manufacturing industry to centimetre accuracy for architecture and construction. We categorize by the amount of images to do measurements on; Single image photogrammetry for single image processing, mono-plotting and orthophotographs. Stereo photogrammetry for dual image processing and stereoscopic measurements. Multi-image photogrammetry for multiple images ($n > 2$) and bundle triangulation.

The recording and processing methods has changed since the first application of this method;

- Plane table photogrammetry: graphical evaluation (until ca. 1930)
- – Analogue photogrammetry: analogue cameras, optomechanical measurement systems (until ca. 1980)
- – Analytical photogrammetry: analogue images, computer-controlled measurement
- – Digital photogrammetry: digital images, computer-controlled measurement

Photogrammetry is a three-dimensional measurement technique which uses central projection imaging as its fundamental mathematical model (Fig. 1.6). Shape and position of an object are determined by reconstructing bundles of rays in which, for each camera, each image point P' , together with the corresponding perspective centre O' , defines the spatial direction of the ray to the corresponding object point P . Provided the imaging geometry within the camera and the location of the imaging system in object space are known, then every image ray can be defined in 3D object space.

Luhmann, 2011

The old analogue system required a high level of expertise, as the images had to be processed manually by experts in a laboratory environment with specialised equipment. It was a time-consuming procedure demanding both specialized knowledge and skills. The digitalization of photogrammetry has changed the process fundamentally, and specialised equipment is replaced by standard computing hardware. The vast amount of automation has allowed for novice users to do both the data recording and evaluation.

Photogrammetry is almost as old as photography itself; the first experiment dated back to 1849 on a picture of a hotel façade. The first photogrammetric camera was used by an architect to measure the exterior of a cathedral. The use of photography was primarily to avoid the dangerous manual measuring method used at the time. In the next decades, the usage spread to other disciplines, and in 1884 Paganini used it to map the Alps. The use of stereography came next with advanced and specialized cameras and plotters.

In 1956 the first papers describing the principle method of bundle adjustment was published, and 12 years later the first commercial programs were available. Luhmann (2011) states “The importance of bundle adjustment in close range photogrammetry can hardly be overstated. The method imposes no restrictions on the positions or the

orientations of the cameras; nor is there any necessity to limit the imaging system to central projection. Of equal or greater importance, the parameters of interior orientation of all the cameras may be included as unknowns in the solution.”

Since then the digital age has dawned upon photogrammetry, and both the cameras and the processing equipment is digital, the program used in this thesis was first released in 2010.

After deciding that photogrammetry be the way forward, the obvious question was which Software to use. Three software packages were considered; Photomodeler Scanner, PhotoScan and Bundler, all with several hits in academic search engines. First trial licenses were obtained; unfortunately Photomodeler Scanner did not want to give me a trial license, based on my description of my project. Bundler had a timeworn GUI, awkward installation procedure and only a command line interface. On the positive side, it was free and distributed under GNU General Public License. However, since I was not able to track down any updates in the software after version 0.4 from 2010, I did not pursue this package any further and uninstalled it. PhotoScan, on the other hand, was readily available in a 30day trial, no questions asked, regularly updated and with a forum with lots of users and quick replies from company employees. The program has support for several export formats, and can do structure from motion (SFM) modelling. After 30 days, a permanent license was obtained, for educational purposes the price was 550 U\$ for the professional version. The standard edition was ruled out mainly because of its lack of measurement and ground control support.

2.1 Hardware

The camera used in this experiment was a Nikon D3200 digital single-lens reflex (DSLR) camera with a 24.2 megapixel CMOS sensor. According to PhotoScan user manual any camera with more than 5 megapixels is sufficient to provide photos to the software. Secondly the D3200 is a low-cost consumer-grade DSLR available for 3500,- nok and fits in my philosophy of doing this project within a low-cost budget without affecting the overall result.

A Nikon WU-1A Wireless Mobile Adapter was used for tethering the camera from an Android device (A Samsung Galaxy Note 10.1 running Android 4.0 was used). On the Galaxy Note, the application qDslrDashboard was used to control the DSLR camera. The application allows for full integration and control with the camera, and also allows for the Android device to be the “host” for the captured pictures. The Galaxy Note tablet was equipped with a Samsung 32 GB micro SDHC EVO memory card for image storage. The memory card has transfer speeds up to 48 MB/s.

A parallel laser device was constructed and tested. It was a printed plastic block with two holes each inserted with a small laser diode. It was designed so that the lasers were parallel with 10 cm between the lights up to a distance of 1.5 m. Unfortunately, one of the laser diodes died in between experiments, so this tool was not used in the final sets of pictures.

A PC with an Intel i7 2600k CPU @ 4.4 GHz, and an NVidia GTX 660Ti graphics card running Windows 7 and the following software: Agisoft PhotoScan Professional Edition, Adobe Lightroom 4.4, Cloudcompare and MeshLab. The recommended setup is minimum an Intel i7, and 12 Gb of RAM (Agisoft LLC, 2014). The machine was bought second hand, and has a total cost of 3500,- nok, and is still classed as adequate for the task at hand. A Soehnle kitchen scale was used to measure the weight of the ice, and a Vernier calliper for measuring size.

3 Method

In this chapter, I will show how 2-D imaging data of ice is processed into a 3D model using Agisoft PhotoScan software. I will also show the integrity of the model by comparing two mesh clouds in Cloudcompare, and measure the volume of the model both in PhotoScan and in MeshLab and compare the result. Finally, I will compare these results with the calculated volume of the ice. I will also show that remotely operating the camera and storing the pictures remotely as they are shot is feasible.

3.1 Ice

The ice used in this experiment was 2.05 Litres of water froze into a solid block of ice at -19°C in a 5 Litres steel cast form, without any lid. The water that was frozen had a salinity of 35 ppm. Saltwater was chosen to achieve a white not totally transparent surface on the ice, as this is the most frequent appearance of marine ice accretion.

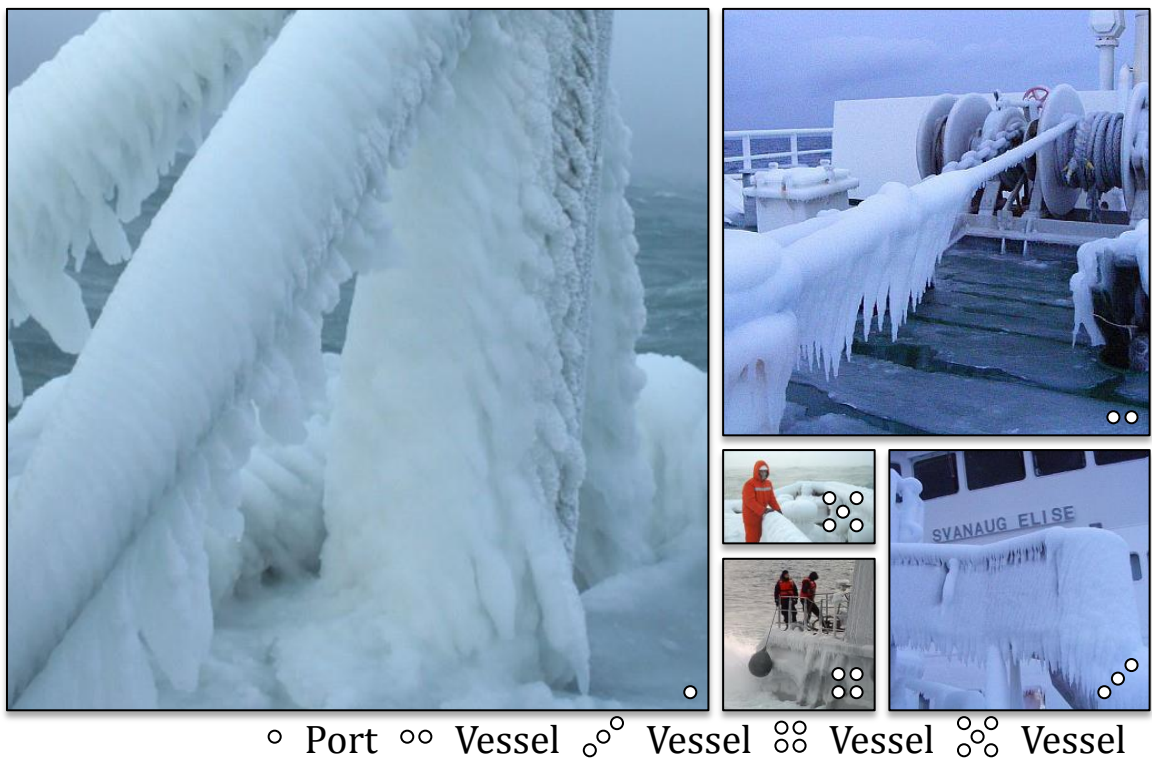


Illustration 5 Marine ice accretion

Pictures are showing the milky white ice accretion on onshore and offshore structures

The form was heated to the ice loosened and placed upside down to free the ice. The bottom of the ice block was evened on a heated steel plate. The purpose of evening was to remove any excess volume introduced to the experiment between the ice and

the surface below caused by the irregular and uneven shape of the free-formed surface. The ice weighed 1914 g after the adjustment.

A set of 24 pictures was taken, and a 3D model created in PhotoScan. The ice was then spray painted with a Plasti Dip rubber coating; this is a no reversible action, and that is why the model had to be created prior to coating. Another 24 pictures was shot of the now blue rubber-coated ice. The rubber coating proved to give a matte surface with a detailed and visible structure. The thickness of the rubber coating is assumed negligible when doing calculations and comparisons. A model of the rubber coated ice was made in PhotoScan.

The density of the ice was calculated from weight and volume of a part of the ice. This part had to be sawed out and afterwards placed in a steel cylinder. The top and bottom was levelled using a warm steel spatula and then frozen again. This process was repeated two times, and the result was an even surface at both ends. The ice was freed from the cylinder weighted and measured. The cylinder was plugged at one end, and filled to the brim with fresh water at 4°C and weighed, the weight of the water corresponding to the volume of the cylinder. A Vernier calliper was used to measure the cylinder and the ice, both of which volume calculated as a control.

3.2 Photography

The primary input to PhotoScan is pictures, and the second chapter of the user manual is devoured to demands and pitfalls for the photogrammetry photographer. For the camera, the need for sharp images, high-resolution, high aperture and low shutter speed are all mentioned. For the scene the following limitations are mentioned:

- Avoid not textured, shiny, mirror or transparent objects.
- Avoid absolutely flat objects or scenes.
- Avoid unwanted foregrounds.
- Avoid moving objects within the scene to be reconstructed.

Taking pictures of ice means that the pictures will be of a shiny, mirror or transparent object, and in this particular case, the scene is flat, but not entirely flat. It should be noted that if the methodology presented in this paper is tested on an outdoor scene precipitation like snow, sleet or hail will be a moving objects in the scene unless there are multiple cameras with synchronized time of capture.

The PhotoScan software works with original images, so do not crop or geometrically transform them. Resizing and rotating are mentioned, but also automatic lens correction like lens vignetting, distortion and chromatic aberration can also change the picture geometry (These are commonly available in photo editing software).

3.2.1 Capturing Photos

On both scenes, the camera (a single camera was used) was placed on a tripod. The camera was elevated, and the centre body of the camera had a height of 55 cm (Centre body assumed to be the location of the image sensor). The Pictures were taken in a circle with 60 cm radius around the ice.

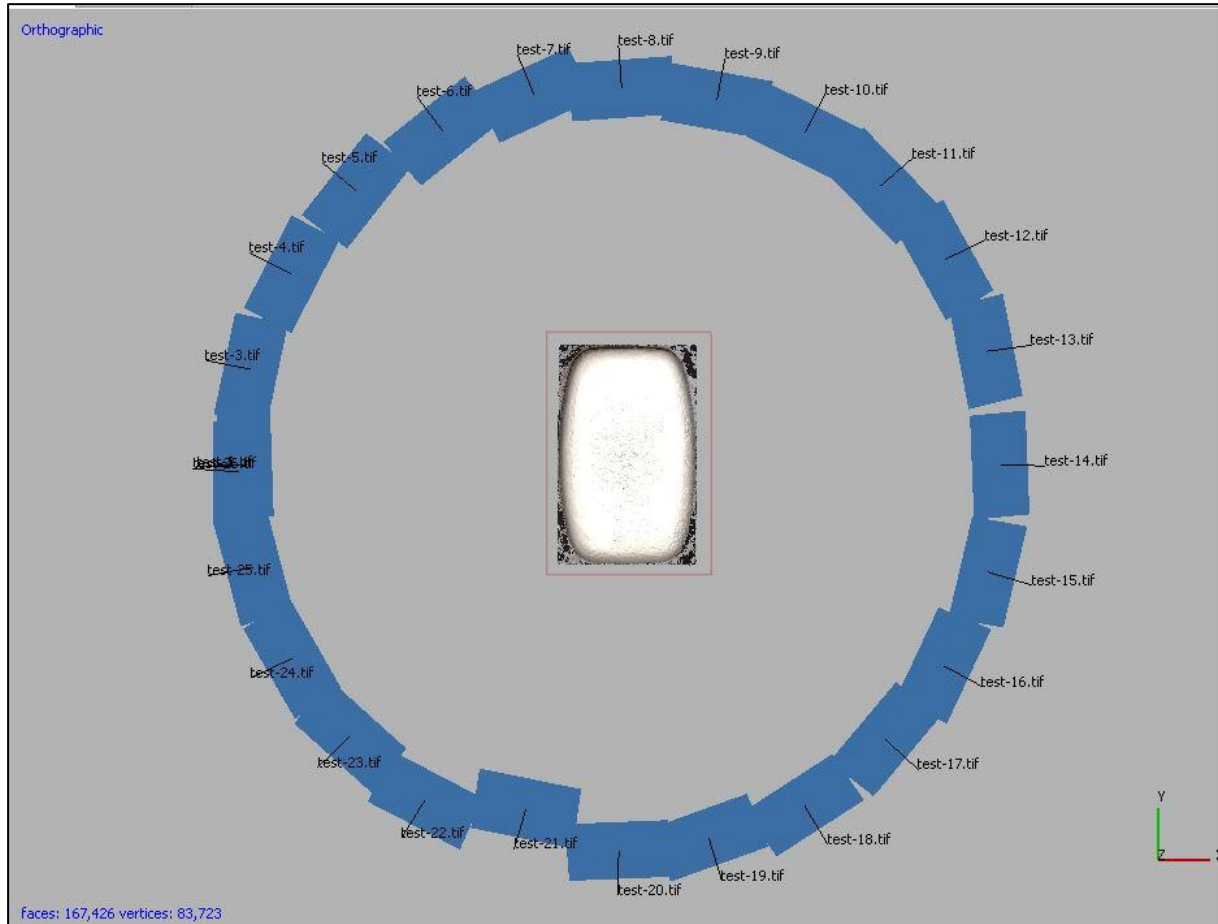


Illustration 6 Camera setup around the ice

The blue squares are each corresponding to a single camera location. It should be noted that the names of the camera are referring to the picture file name

For each picture the camera was moved 15.7 cm along the perimeter of the circle, this corresponds to a 15° movement and adds up to a total of 24 images in each scene. For every trial, the pictures taken were named, and image sequence number and the different photo sets were separated into folders.

This setup was chosen according to the PhotoScan software manual; Illustration 7, next page, showing the correct setup for isolated objects.

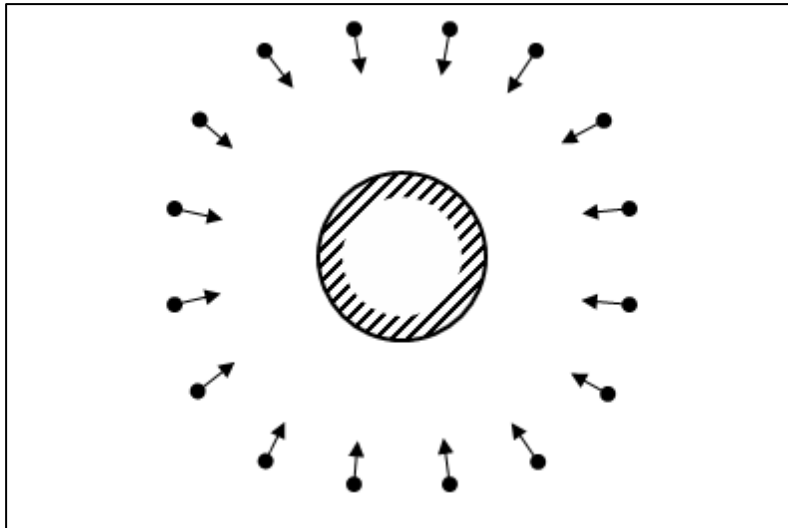


Illustration 7 Correct camera setup for isolated object

The exact location of the camera in each shot was measured and recorded in a local grid and a text file consisting of these coordinates and was imported into PhotoScan. It is recommended to use either marker with known distance on the object or to place a ruler within the shooting area. Placing a ruler was not done because it would have defeated the purpose of the experiment, trying to create a 3D model of a translucent surface (Perovich, 2003).

To verify that adding a measuring rule foreign to the scene added details that else would not be present, the built-in image quality estimation tool in PhotoScan was used. The image quality numbers were 0.805 versus 0.313, a higher number is better, where the picture with the higher number was the one to the left (with a ruler). This implies that the ruler adds detail to the picture and that the decision to avoid using it was correct.



Illustration 8 Images used for comparison of image quality

Most digital cameras today have a “Live view” option. With this enabled you can see the scene being shot on a small digital screen and review the picture after capture. For Nikon DSLR cameras the screen is normally in the region from 3-3.5 inches (for example does the high end professional grade Nikon 810 launched in Q3 2014 come with a 3.2” LCD (NIKON Web)). Reviewing sharpness in details on small screens was experienced to be time-consuming. Therefore, it was decided to utilize a Nikon WU-1a Wifi adapter in conjunction with the Android application qDslrDashboard allowing for full remote access and control of the camera. By using a 10.1” notepad the scene was viewed in “live view” before shooting the picture and the resulting photo, was reviewed on a large screen with easy touchscreen control and high resolution. This way the photographer can determine whether the photos taken are acceptable for input into PhotoScan.

The remote control also introduces another benefit, as pressing the manual shutter on the camera can introduce movement. Controlling the camera from another device eliminates this risk of this.

3.2.2 Pictures file format

The pictures used in this experiment were shot in NEF format. NEF is a proprietary format exclusively for Nikon Cameras (Langford, Fox, & Smith, Langford's Basic Photography, 2007) and contain RAW image data without any compression. From a photographer's viewpoint, this is standard procedure shooting with a DSLR camera, as the only disadvantage is that RAW pictures take up much space on the memory card. The advantage is that no data is lost in compressing the image and changing exposure (Ibid). Post-processing is also readily available to enhance the photo. The RAW file size was 20-24 Mb per photo, and for the TIFF uncompressed 38-53 Mb. The Hardware and software used had no problems handling these file sizes. PhotoScan is not able to import NEF files, so these had to be converted. For the conversion, Adobe Lightroom 4.4 was used. The export format selected was TIFF uncompressed. File format decisions were made on recommendations in the Agisoft PhotoScan User manual. (Agisoft LLC, 2014)

No geometrical modification was applied in Lightroom, but all pictures had the autotune feature enabled, which can make changes to Exposure, Contrast, highlights, shadows, whites and blacks.

3.2.3 DOF and Aperture

Pictures used in photogrammetry should be as sharp as possible to obtain a good result. (Agisoft LLC, 2014) It is common knowledge that pictures do not go from sharp to unsharp instantly but rather deteriorates slowly from one to the other. In photography, the range of scene depths perceived as sharp are said to be in focus, and the ranges of depths in the picture that are in focus are called depth of field. The DOF can be theoretically calculated using a DOF calculator; the inputs are camera brand and model, lens focal length and aperture and finally distance to the object being captured. Illustration 9 is captured by the same lens and camera at the same distance to the target and with the same aperture as used in the experiment on the ice, and clearly shows that DOF affects the photo. In the picture it is clear that 3-4 lines of text are in sharp focus (Blue) and the two adjacent lines above and below are slightly blurred (red), but still readable. The lines then gradually deteriorates (yellow) to not readable text (black) at the edges of the photo.

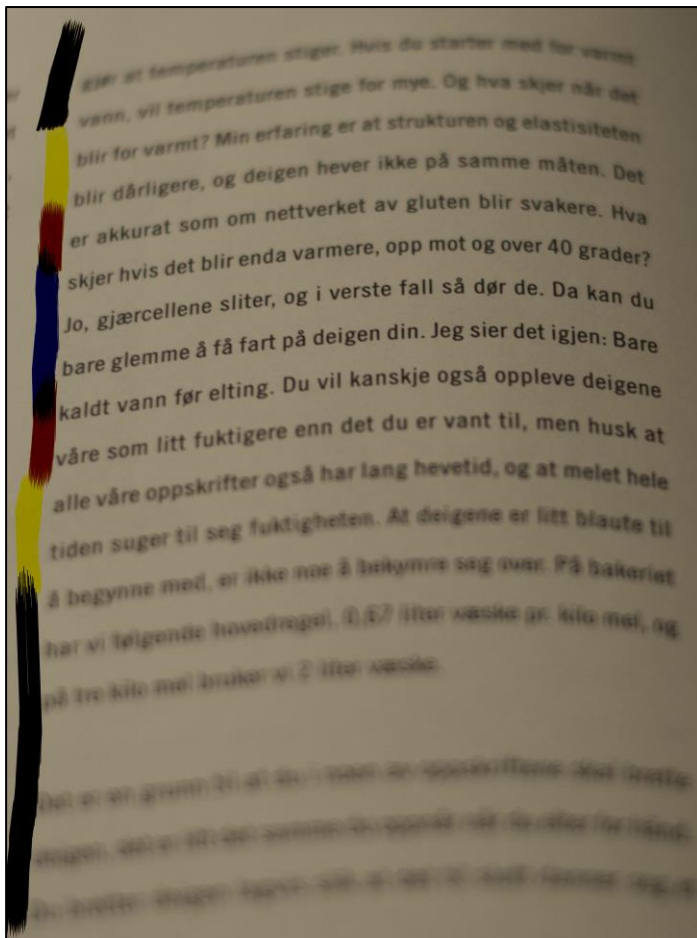


Illustration 9 Depth of Field

Picture showing how depth of field affects text in a picture

The qDSLRdashboard comes with an integrated DOF calculator, and this was used to calculate the DOF for this experiment.

| Distance | F-Stop | Near-DOF | Far-DOF | Total |
|----------|--------|----------|---------|--------|
| 0.40 m | f/1.8 | 39.8 cm | 40.2 cm | 0.4 cm |
| 0.40 m | f/2.8 | 39.7 cm | 40.3 cm | 0.6 cm |
| 0.45 m | f/1.8 | 44.7 cm | 46.3 cm | 0.5 cm |
| 0.45 m | f/2.8 | 44.6 cm | 45.4 cm | 0.8 cm |
| 0.50 m | f/1.8 | 49.7 cm | 50.3 cm | 0.6 cm |
| 0.50 m | f/2.8 | 49.5 cm | 50.5 cm | 1.0 cm |

Table 1 DOF calculation

A table showing how DOF varies depending on object distance and aperture

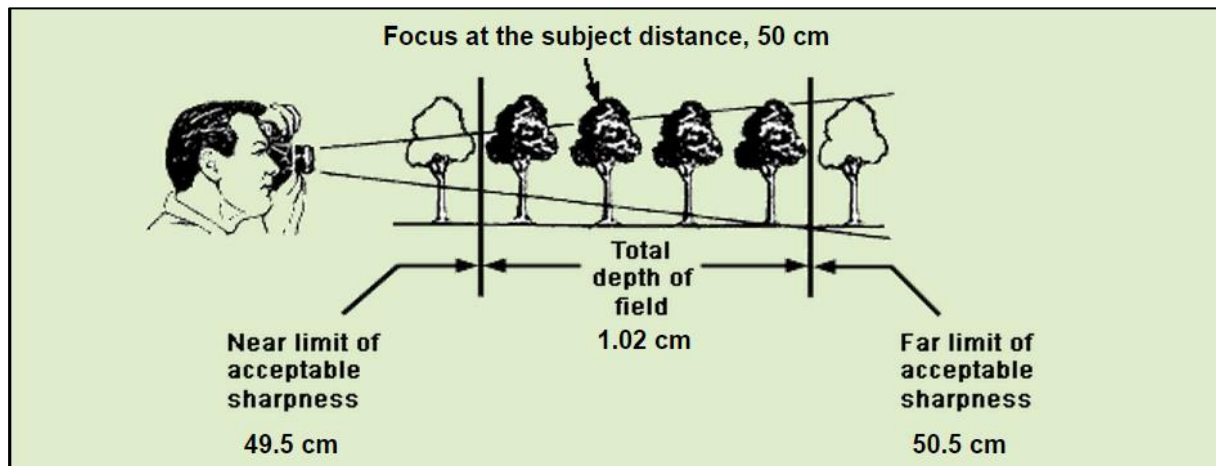


Illustration 10 DOF at 0.5 m f-stop f/2.8

The acceptable sharpness is a term called “circle of confusion”, which is defined by how much a point can be blurred in a photo, in order to perceive it as unsharp. Camera manufacturers assume it to be negligible if it on an 8*10inch viewed from 1foot is less than 0.01 inch. The PhotoScan SW is still able to identify points when this blurry, so the DOF table values are not absolutes, but guidelines to identify possible areas with inadequate coverage. DOF is dependant of aperture, which in layman’s terms is the size of the hole that lets light pass through the lens and on the image sensor. It works similarly as the pupil of the human eye. As seen in Illustration 11, larger f numbers indicate bigger opening and results in a shorter DOF. Smaller f-numbers have the opposite effect and increase the DOF. For pictures in low lighting conditions or substantial movement, the general recommendation is to use a large f-number (i.e. f/1.4).This allows more light to strike

the sensor in a shorter time span, and the result is sharper pictures. If a larger f-number is chosen, this can be countered with higher light sensitivity (ISO setting) or longer exposure. The higher ISO setting leads to more noise in the picture, and longer exposure (shutter speed) leads to noise if there is movement. (Langford, Fox, & Smith, Langford's Basic Photography, 2007) So for any camera on a floating installation or vessel this would lead to more noise and blurry pictures. PhotoScan can correct for this, if the values are known.

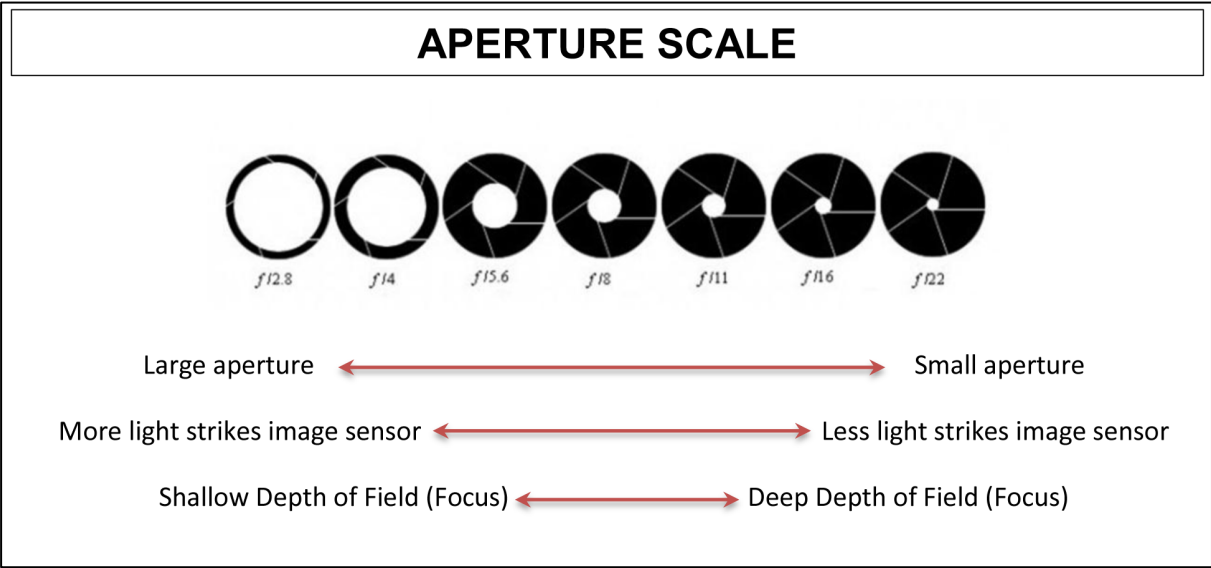


Illustration 11 Aperture

Visualization of aperture with a five blade iris control and relationship with DOF and light on the sensor

3.2.4 Camera Lens and Blitz

The lens used in this experiment is a Nikkor 50mm 1:1,8G from Nikon. The user manual states that fixed lenses are preferred, and that the best choice is 50 mm focal length (35 mm film equivalent). The lens has autofocus and a maximum aperture of f/1.8 and a minimum focus distance of 0.25 m (Nikon, 2014).

At first the experiment was done with an 18-55mm f3.5-5.6G lens, but this proved to be insufficient for indoor photography, the lens was not able to autofocus, and the pictures ended up grainy.

In this experiment, it was decided not to use the built-in or an external Blitz. The ice surface would be lit up from different angles, causing the surface look different on every shot and the PhotoScan SW would have problems identifying common points. Also shooting pictures in any precipitation (especially sleet or snow) or sea spray with blitz will cause immediate reflections, illustration 12. Neither blitz nor blinking lights are recommended according to the user manual.



Illustration 12 Blitz used in snowfall

The picture is showing how blitz reflections in snowflakes that dominate the picture.

3.3 Agisoft Software

In this chapter, the Agisoft PhotoScan software will be presents, and the relevant procedures to achieve a 3D model. My thesis has been ongoing for a prolonged period, in which there have been several updates to the PhotoScan software. The results I refer to in this thesis were achieved using the 1.1.5, but my initial research started with version 0.9.0. Build 1586. Several of these updates have refined and improved the different steps in the process that at the time prohibited this project to advance. Improvements in the image alignment phase have proven vital for the possibility to create 3D models of ice. The last version available 1.1.5 was installed in April 2015 and all model re-run on this new version, neither the changes log or the user manual have been updated to reflect the changes made to this version. The development of this software has been tremendous, since January 2014 there has been nine major releases, many of which have changed the user input options and speeded up the computations. For instance, the average dense cloud computations were reduced from an average of 4500 seconds in version 0.9.1 to an average of 230 in version 1.1.5 for a medium quality cloud on the system in use. This has proven to be a challenge, as this research is based on a newer software version than what is referred to by others using the PhotoScan software, and subsequently have other options and features available. For example did the Camera Scale bar first appear in the 1974 build, which was a preview edition, from September 2014. The official updated edition came in December 2014 (Build 2004), less than four months ago. Agisoft have an updated Community forum hosted on their website that have both other users and company representatives replying to problems and questions asked there, this has been a valuable source of information and help when using the software.

3.4 Agisoft PhotoScan

The 3D models were generated using Agisoft PhotoScan Professional Edition, version 1.3.5 - 64 bit, build 2034 on a Windows 7 Ultimate 64 bit OS. PhotoScan is 3D model generation software developed and distributed by the Russian-based company Agisoft LLC. The program is capable of transforming multiple 2D images into a precise 3D model in a 3 step process. (Verhoeven, 2011) Being a commercial product, the algorithm's performing the different operations in the background are not available to the public. Company representatives stated on the user forum that "we have favoured algorithms with higher accuracy output over faster approaches with less accurate output" (Semyonov, 2011). The primary input to PhotoScan is pictures, and the second chapter of the user manual is devoted to demands and pitfalls for the photogrammetry photographer. For the camera, the need for sharp pictures, high-resolution, high aperture and low shutter speed are all mentioned. For the scene the following limitations are mentioned:

- Avoid not textured, shiny, mirror or transparent objects.
- Avoid absolutely flat objects or scenes.
- Avoid unwanted foregrounds.
- Avoid moving objects within the scene to be reconstructed.
- Number of photos: more is better than less
- Geometry to be reconstructed has to be visible on minimum two pictures
- Good overlap between photos is crucial for the result.

The ice surface is translucent, and cannot be changed, but the other demands were fulfilled with the setup chosen for this experiment. Picture EXIF data (image metadata) is an essential component for solving camera position and orientation, and it is vital that this information be present in the images to be aligned in PhotoScan. See Appendix 1 for a full EXIF data extraction.

According to Verhoeven (2011) PhotoScan utilizes a state-of-the-art SFM (structure for motion) algorithm. SFM is a method similar to Stereoscopic photogrammetry, but differs fundamentally from conventional photogrammetry in one aspect; the geometry of the scene. Camera pose and scene geometry are reconstructed simultaneously using feature matching from overlapping photos (M.J. Westoby, 2012). The resulting 3-D point cloud derived will, therefore, lack both scale and orientation. These can be

obtained either by using minimum GCP or exact camera location (orientation is not needed). For the purpose of this study, the latter was used.

The software support OpenCL for devices supporting this technology, in short, OpenCL exploits GPU processing powers to speed up calculations. Prior to PhotoScan version 1.1.3 the computer and GPU on the machine in use was not able to utilize this feature, even though the hardware supported this. The program would return an error message and do only CPU calculations. For dense cloud computations, this would total to 109 million samples per second and a processing time of 425 seconds for the 25 pictures used in this experiment. After installing version 1.1.3, this processing time was significantly reduced. The dense cloud processing now did 523 million samples per second and a processing time of 222 seconds. The increase in samples per second is caused by GPU calculations alone. To utilize the OpenCL feature, the user must manually enable it in program preferences. At the same time, it is recommended to free up one CPU core (two if multithreading is enabled) per GPU device. The freed CPU core is used for control and management tasks. For this experiment, the OpenCL was enabled, and 6 of 8 CPU cores were set to active. A processing log was enabled, and so was VBO support. Other than that the default settings were kept. The 3-D reconstruction is based on a 3 step process;

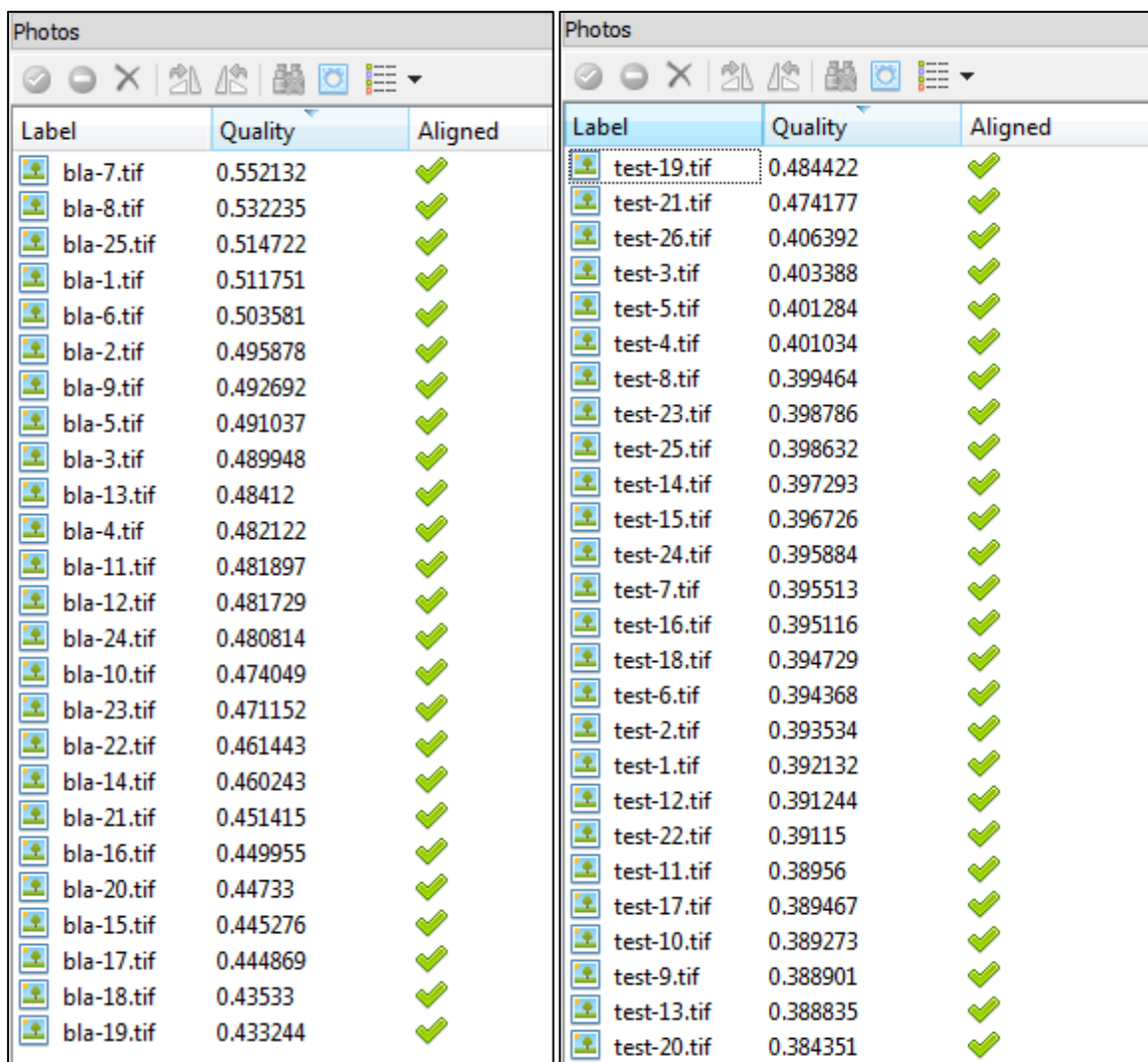
- Align Photos
- Build dense cloud
- Build Mesh

There is also an option to build texture, but for the purpose of volume calculation this is not relevant. For this experiment, three 3-D models were created out of 2 sets of photographs. Two of the models contained the whole image scenery of each photo set. The third model was of the white ice only; all other features were masked out of the photographs.

3.5 Workflow in PhotoScan

3.5.1 Loading photos

The first step in PhotoScan is to load and review all photos. In the software, all photos are called cameras, and they are loaded into chunks. Chunks are used to discriminate pictures taken with different cameras/lenses, at different heights or if there is a need to apply different processing regimes for parts of the photoset. Since none of the above applied to the pictures taken, they were all processed in the same chunk. PhotoScan has a built in quality estimation feature, and all the photos were checked. According to the user manual, the pass criteria is a value higher than 0.5.



| Label | Quality | Aligned |
|------------|----------|---------|
| bla-7.tif | 0.552132 | ✓ |
| bla-8.tif | 0.532235 | ✓ |
| bla-25.tif | 0.514722 | ✓ |
| bla-1.tif | 0.511751 | ✓ |
| bla-6.tif | 0.503581 | ✓ |
| bla-2.tif | 0.495878 | ✓ |
| bla-9.tif | 0.492692 | ✓ |
| bla-5.tif | 0.491037 | ✓ |
| bla-3.tif | 0.489948 | ✓ |
| bla-13.tif | 0.48412 | ✓ |
| bla-4.tif | 0.482122 | ✓ |
| bla-11.tif | 0.481897 | ✓ |
| bla-12.tif | 0.481729 | ✓ |
| bla-24.tif | 0.480814 | ✓ |
| bla-10.tif | 0.474049 | ✓ |
| bla-23.tif | 0.471152 | ✓ |
| bla-22.tif | 0.461443 | ✓ |
| bla-14.tif | 0.460243 | ✓ |
| bla-21.tif | 0.451415 | ✓ |
| bla-16.tif | 0.449955 | ✓ |
| bla-20.tif | 0.44733 | ✓ |
| bla-15.tif | 0.445276 | ✓ |
| bla-17.tif | 0.444869 | ✓ |
| bla-18.tif | 0.43533 | ✓ |
| bla-19.tif | 0.433244 | ✓ |

| Label | Quality | Aligned |
|-------------|----------|---------|
| test-19.tif | 0.484422 | ✓ |
| test-21.tif | 0.474177 | ✓ |
| test-26.tif | 0.406392 | ✓ |
| test-3.tif | 0.403388 | ✓ |
| test-5.tif | 0.401284 | ✓ |
| test-4.tif | 0.401034 | ✓ |
| test-8.tif | 0.399464 | ✓ |
| test-23.tif | 0.398786 | ✓ |
| test-25.tif | 0.398632 | ✓ |
| test-14.tif | 0.397293 | ✓ |
| test-15.tif | 0.396726 | ✓ |
| test-24.tif | 0.395884 | ✓ |
| test-7.tif | 0.395513 | ✓ |
| test-16.tif | 0.395116 | ✓ |
| test-18.tif | 0.394729 | ✓ |
| test-6.tif | 0.394368 | ✓ |
| test-2.tif | 0.393534 | ✓ |
| test-1.tif | 0.392132 | ✓ |
| test-12.tif | 0.391244 | ✓ |
| test-22.tif | 0.39115 | ✓ |
| test-11.tif | 0.38956 | ✓ |
| test-17.tif | 0.389467 | ✓ |
| test-10.tif | 0.389273 | ✓ |
| test-9.tif | 0.388901 | ✓ |
| test-13.tif | 0.388835 | ✓ |
| test-20.tif | 0.384351 | ✓ |

Illustration 13 Image quality estimation

The image quality for the two datasets used, ice with rubber coating to the left, sorted from high to low.

The image quality for the two datasets shows that a majority of the pictures has a value below 0.5. The explanation being a shorth DOF, but the picture of the blue

rubber-coated ice with lowest quality has better quality than 24 of the 26 pictures of the ice. Lens calibration figures from Agisoft lens were loaded. The values are used as initial data prior to the SFM 3-D reconstruction applied in the Align photos, see illustration 14.

The screenshot shows a software interface for lens calibration. At the top, 'Camera type' is set to 'Frame'. Below it, 'Pixel size (mm)' is 0.00385319 x 0.00385319, and 'Focal length (mm)' is 50. There are two tabs: 'Initial' and 'Adjusted', with 'Adjusted' being the active tab. Under the 'Adjusted' tab, the 'Type' is 'Precalibrated'. The parameters are as follows:

| Parameter | Value |
|-----------|--------------|
| fx: | 14735.9 |
| fy: | 14731 |
| cx: | 2926.24 |
| cy: | 1997.7 |
| skew: | 0 |
| k1: | -0.159676 |
| k2: | 0.26082 |
| k3: | -5.56397 |
| k4: | 0 |
| p1: | -8.87987e-05 |
| p2: | 0.000309183 |

There is also a checkbox labeled 'Fix calibration' which is currently unchecked.

Illustration 14 Lens calibration values applied

The measured camera positions were imported. They were organized in a tabulator separated file, see Appendix 2. The positions are in a local coordinate system, and the coordinate is given in hundredths of a meter (i.e. cm). A common problem, also experienced by me, is that the x and y coordinates are mixed up, causing the z-value to be inverted, this is discussed in 2.7.

When creating a 3-D model based solely on the white ice in the photos, PhotoScan applied masks onto all other features. The masks are applied manually to each photo; this is a time-consuming process and has to be done prior to the photo alignment.



Illustration 15 Picture with the mask applied.

The mask is applied manually on every single photo

The mask is stored in PNG file format and is black and white. The white is the area to be used for modelling, the black indicate the area to be excluded.

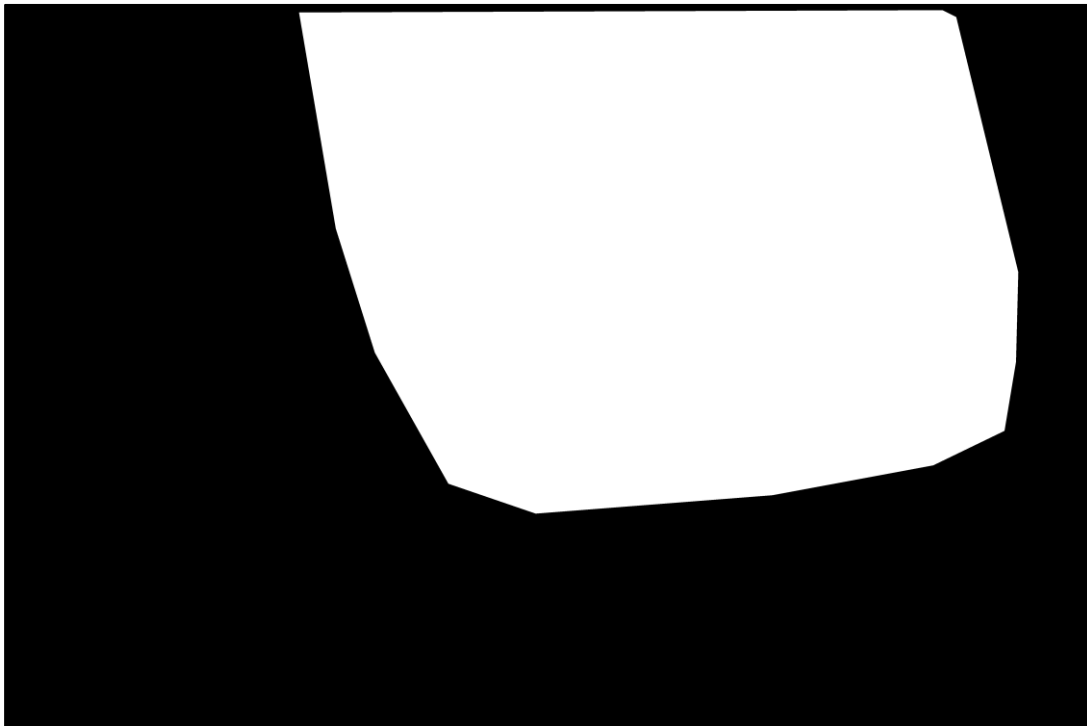


Illustration 16 Mask file

3.5.2 Align photos

The photos were then aligned with high accuracy, using the reference pair preselection option. Allowing the software to use camera locations to work out picture overlaps, speeds up the pair selection. It will also give the Mesh cloud scale and orientation. There are three settings on accuracy, high, medium and low. The effect of choosing a lower accuracy is shorter processing time and lower camera accuracy. The processing time for the camera alignment at high accuracy was less than 2 minutes, and reducing the accuracy for this experiment was not even considered based on this. To allow for mask, the tick box Constrain features by mask has to be chosen manually.

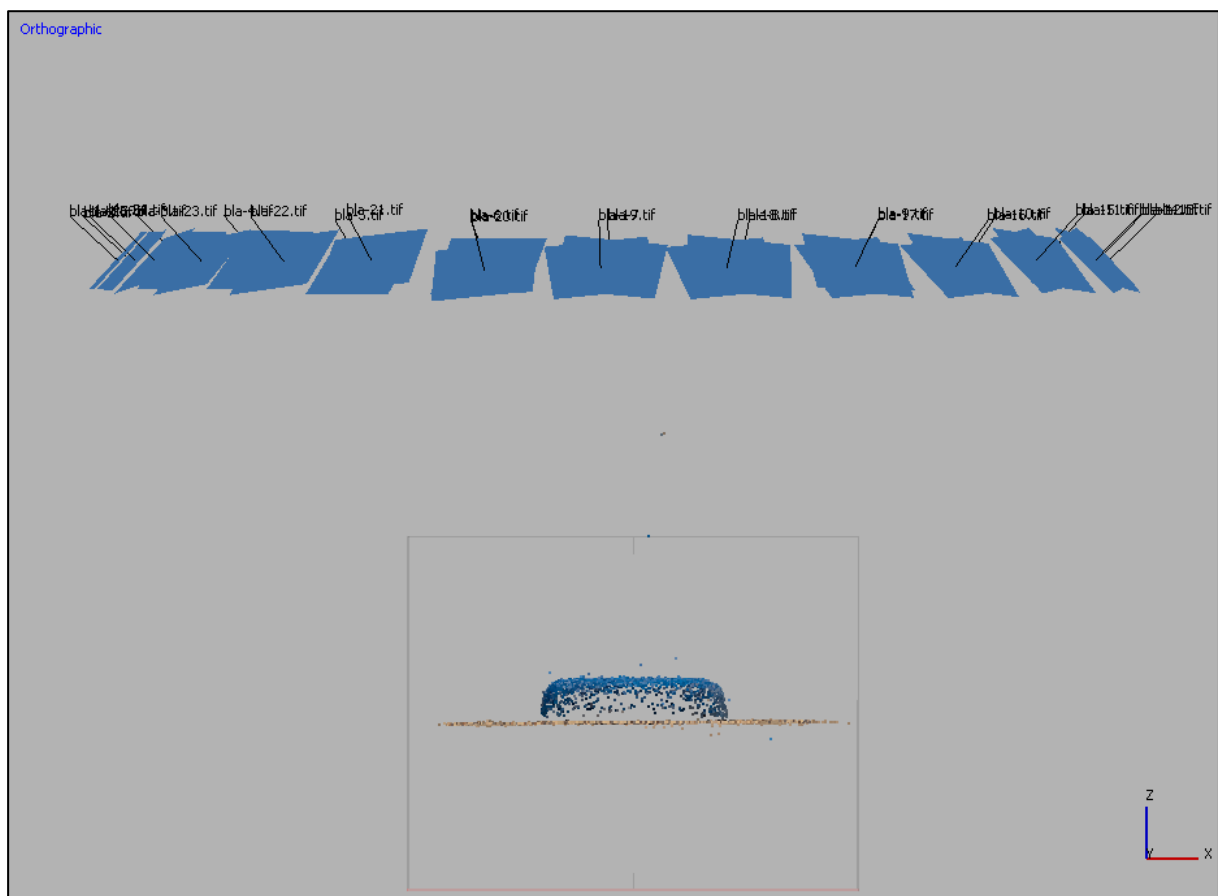


Illustration 17 Sparse point cloud

The estimated camera locations are clearly visible

The photos are analysed, and feature points detected and matched with overlapping photos. The alignment then computes a sparse point cloud based on camera pose and valid feature points. The cloud, scene orientation (orientation is the axis symbol in the lower right-hand corner) and camera locations are clearly visible.

A table of estimated errors for all cameras is also available see illustration 18; it is computed based on the camera location info imported into the program. It should be noted that since all cameras are at the same height, it was experienced that the errors for the z value was for inter-camera positioning only. By accident, the z-value was set to 45 not 55 on a test model, and the errors remained the same, but the model was moved 10 centimetres below the z-plane. This error was rectified, and the correct height applied.

| Cameras | X err (m) | Y err (m) | Z err (m) | Error (m) | Y |
|--|-----------------|-----------------|-----------------|-----------------|---|
| <input checked="" type="checkbox"/> bla-1.tif | -0.001684 | 0.000124 | 0.001127 | 0.002030 | |
| <input checked="" type="checkbox"/> bla-2.tif | 0.003238 | 0.003204 | 0.000629 | 0.004599 | |
| <input checked="" type="checkbox"/> bla-3.tif | 0.001938 | -0.000835 | 0.001174 | 0.002415 | |
| <input checked="" type="checkbox"/> bla-4.tif | -0.005073 | 0.003124 | 0.001815 | 0.006228 | |
| <input checked="" type="checkbox"/> bla-5.tif | 0.004471 | 0.001074 | -0.003219 | 0.005613 | |
| <input checked="" type="checkbox"/> bla-6.tif | 0.000392 | 0.002684 | -0.002452 | 0.003656 | |
| <input checked="" type="checkbox"/> bla-7.tif | -0.001350 | 0.001484 | -0.002951 | 0.003569 | |
| <input checked="" type="checkbox"/> bla-8.tif | 0.001267 | 0.002112 | -0.002250 | 0.003336 | |
| <input checked="" type="checkbox"/> bla-9.tif | 0.000690 | -0.004812 | -0.001402 | 0.005059 | |
| <input checked="" type="checkbox"/> bla-10.tif | -0.004182 | 0.000929 | -0.000789 | 0.004356 | |
| <input checked="" type="checkbox"/> bla-11.tif | 0.001593 | -0.004668 | 0.002659 | 0.005604 | |
| <input checked="" type="checkbox"/> bla-12.tif | -0.004978 | 0.000871 | 0.003170 | 0.005966 | |
| <input checked="" type="checkbox"/> bla-13.tif | -0.000259 | -0.000913 | 0.003188 | 0.003326 | |
| <input checked="" type="checkbox"/> bla-14.tif | 0.002462 | 0.001938 | 0.002778 | 0.004187 | |
| <input checked="" type="checkbox"/> bla-15.tif | 0.004715 | -0.000123 | 0.002673 | 0.005421 | |
| <input checked="" type="checkbox"/> bla-16.tif | -0.001054 | -0.005117 | -0.002724 | 0.005892 | |
| <input checked="" type="checkbox"/> bla-17.tif | 0.000302 | 0.002410 | -0.002673 | 0.003612 | |
| <input checked="" type="checkbox"/> bla-18.tif | -0.001039 | 0.002892 | -0.003162 | 0.004409 | |
| <input checked="" type="checkbox"/> bla-19.tif | -0.000916 | 0.002405 | -0.002834 | 0.003828 | |
| <input checked="" type="checkbox"/> bla-20.tif | 0.002416 | 0.001454 | -0.004593 | 0.005389 | |
| <input checked="" type="checkbox"/> bla-21.tif | -0.002295 | 0.002347 | 0.002875 | 0.004364 | |
| <input checked="" type="checkbox"/> bla-22.tif | 0.002921 | -0.002501 | 0.001537 | 0.004142 | |
| <input checked="" type="checkbox"/> bla-23.tif | -0.003670 | -0.004240 | 0.001427 | 0.005786 | |
| <input checked="" type="checkbox"/> bla-24.tif | 0.000923 | -0.000940 | 0.002274 | 0.002628 | |
| <input checked="" type="checkbox"/> bla-25.tif | -0.000830 | -0.004904 | 0.001723 | 0.005264 | |
| Total Error | 0.002667 | 0.002756 | 0.002496 | 0.004575 | |

Illustration 18 Camera estimated errors

For any model that is to be used for calculations Agisoft recommends optimizing the camera location prior to building the dense cloud, this recommendation was implemented for all three models created. “During this optimization PhotoScan adjusts estimated point coordinates and camera parameters minimizing the sum of reprojection error and the reference coordinate misalignment error.” (Agisoft LLC,

2014). It was experienced that without optimizing camera positions, the volume of the mesh would be oversized with 70-120 ml depending on the model. At this stage, the point matches on each photo can also be inspected.



Illustration 19 Feature point matches with masks enabled

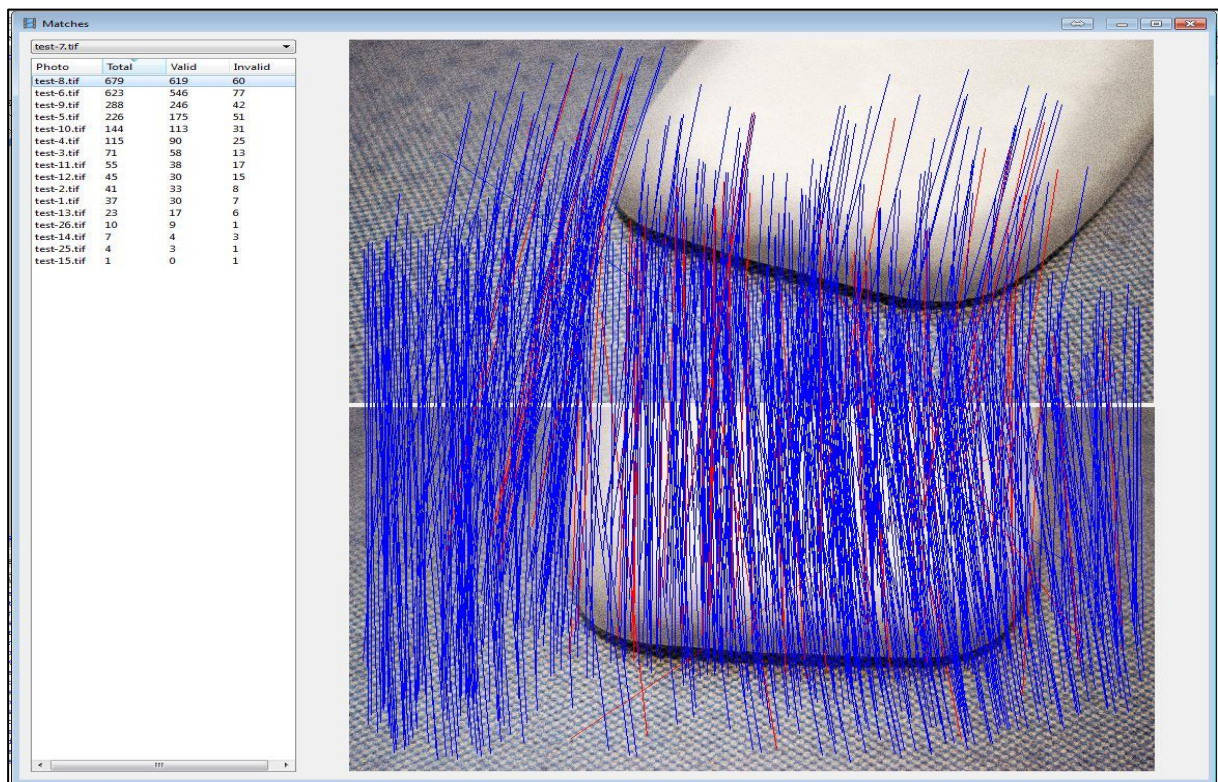


Illustration 20 Feature point matches without masks enabled

On illustration 19 (top) the valid matching feature points between photograph 7 and 8 are blue lines, the reds are invalid. The photos had masks enabled; that is why there are no matches on the features surrounding the ice. Illustration 20 shows the increase in feature points detected outside the ice when mask are not enabled.

3.5.3 Build dense cloud

When building a dense cloud, there are two options, quality and depth filtering.

Quality is a trade-off between detail and time, where the maximum setting is Ultra high, stepping down to Lowest in a total of 5 steps. Ultra high means processing original photos, and each step down downscales the pictures by a factor of 4. This also affects the size of the dense point cloud, and will affect both memory usage and processing mesh building times. Depth filtering is an outlier detection filter that can be set in 4 modes, from Aggressive to disabled. Aggressive was used since the ice surface was known to be without any small detail. Test on Mild and moderate filtering were done, but they did not reveal any details lost by using Aggressive in this particular experiment.

As most of this experiment has been ongoing without OpenCL available, the processing time alone prohibited any attempt to solve at qualities higher than medium. One attempt to build an Ultra high-quality cloud using 26 photos took 17 hours, even a high-quality model is estimated to more than 5 hours processing. Based on this experience the Medium quality was used throughout the extent of this experiment. Even with OpenCL support on the available computer used, the processing time for a dense cloud at high quality is 45 minutes, and building a mesh based on this cloud is another 30 minutes.

3.5.4 Build Mesh

The last step in the 3-D generation is building a mesh. A mesh is a collection of vertices, edges and faces. An edge consists of two vertices, and a face is the area bound by three edges. In PhotoScan, the resulting 3-D model is created of a mesh created from the dense cloud. It is possible to create the mesh from the sparse cloud, but that will generate a lower quality model. There are two different surfaces available, height field and arbitrary. Height field should only be used for planar surfaces where there is only one Z-value for any (X, Y) position. Arbitrary does not make any assumptions about the surface and should be used for any other object. For this experiment arbitrary surface was selected, and medium sized cloud. The amount of faces (polygons) in the mesh is dependant of the amount of points in the dense cloud; hence the mesh of the ice is 30% smaller than the mesh of ice and surroundings.

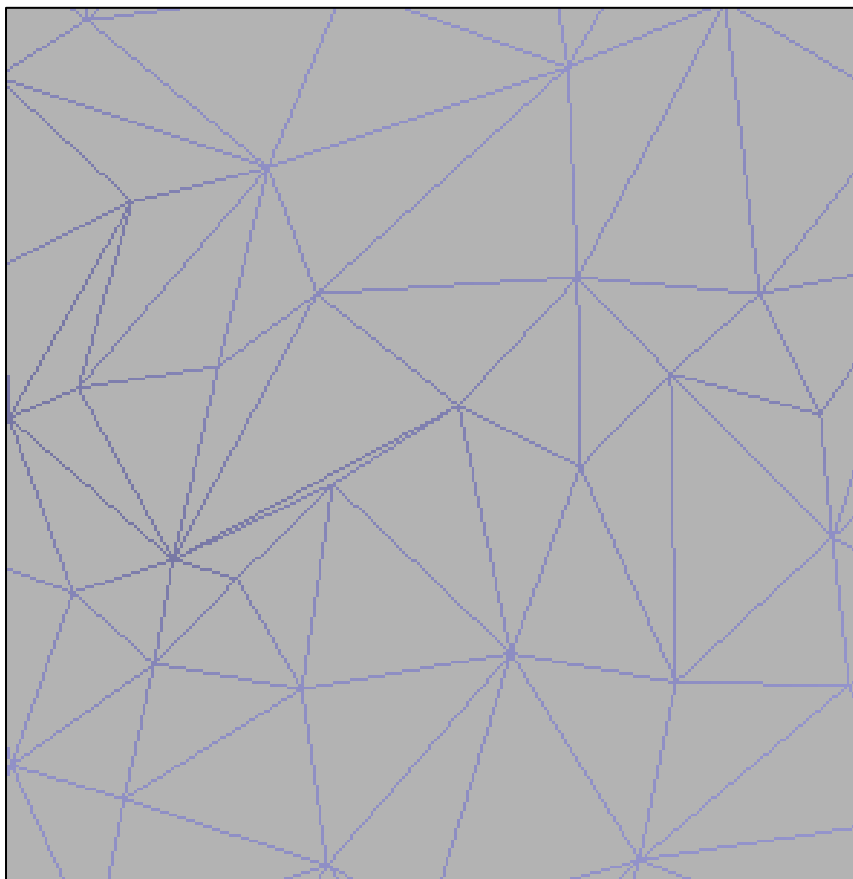


Illustration 21 Mesh

The mesh of a model created in PhotoScan enlarged for displaying purposes

3.5.5 Volume calculations

PhotoScan offers the possibility of volume measurement, but it will only calculate the volume of a closed geometry. For geometry with holes, the program needs to close them first, and then do the calculation.

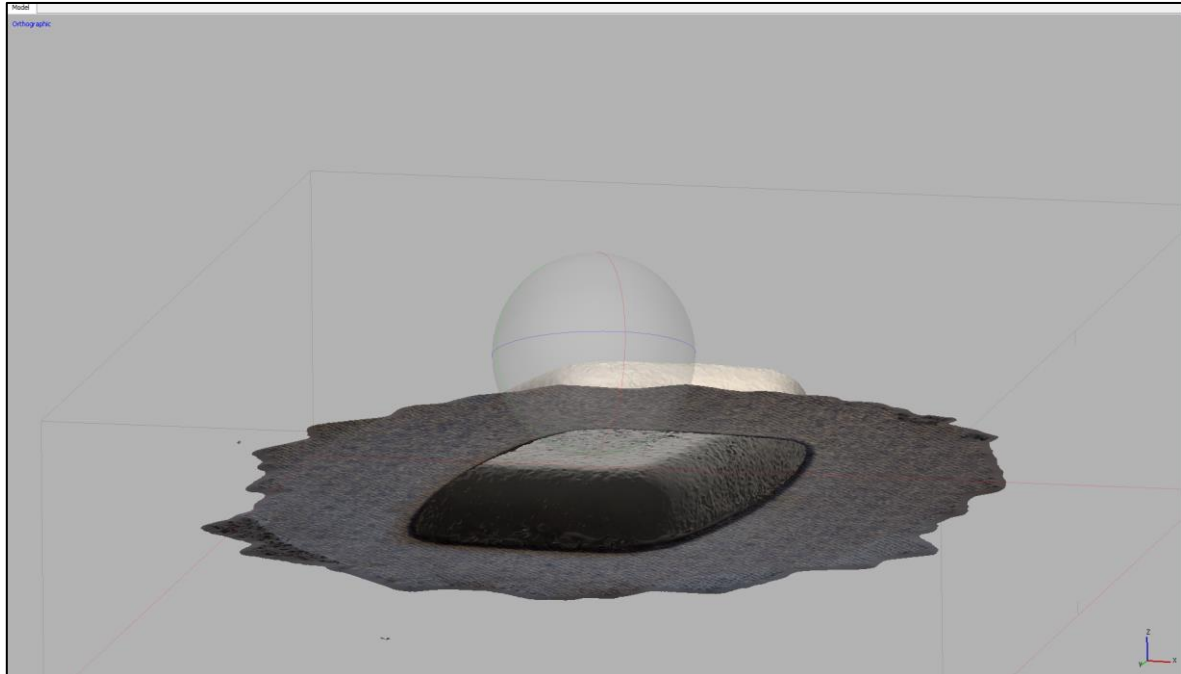


Illustration 22 3-D model of ice

The model is seen from below the ground, and it is clearly visible that it is open at the bottom

The calculation is a manual 2 step process, but care need to be applied when closing the geometry. Since the model has limited overlap at the edges combined with no GCP there apparently is a slight dip on the ground plane towards the edge, illustration 23, below. When closing holes the program use edge to edge as the perimeter of the hole. With a slight dip, there will be excess volume created under the model.

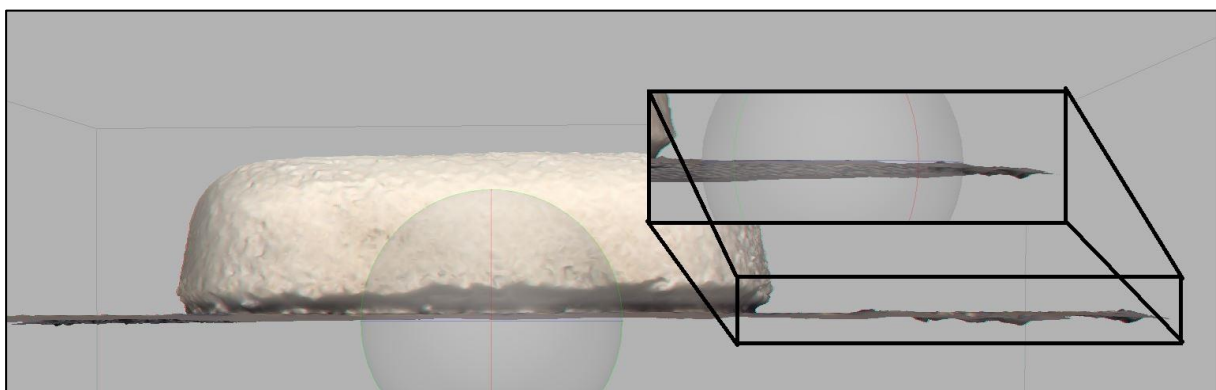


Illustration 23 Slight dip at the edge of the model

To counter this problem, there are two solutions. Either an edit of the model after the mesh has been created. Alternatively, the whole bounding box that indicates the area of interest can be set firmly around the model before building the dense cloud.

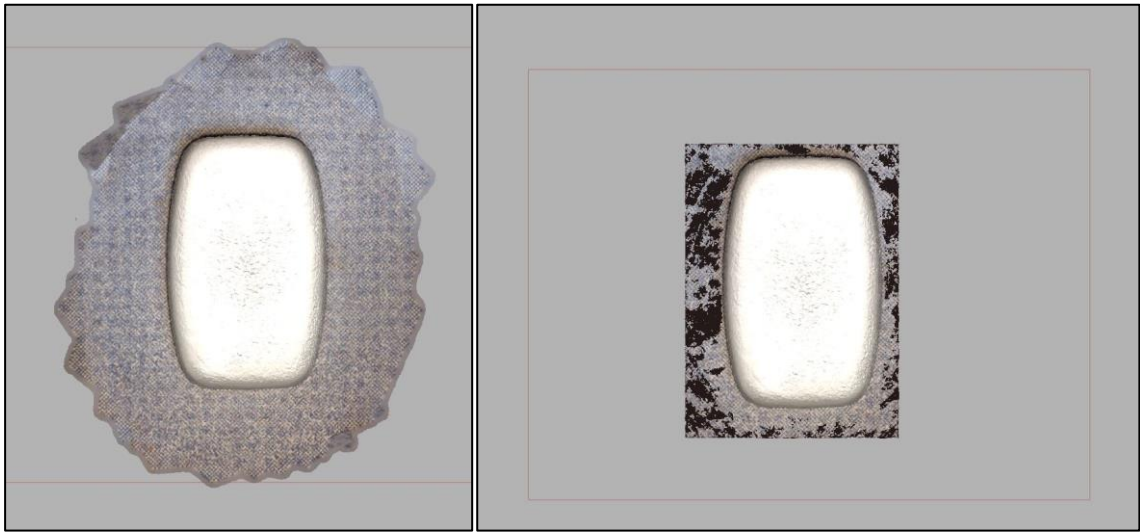


Illustration 24 Before and after cropping the model

The latter is the preferred option if the area of interest is known because it reduces the dense cloud and mesh calculation size and time.

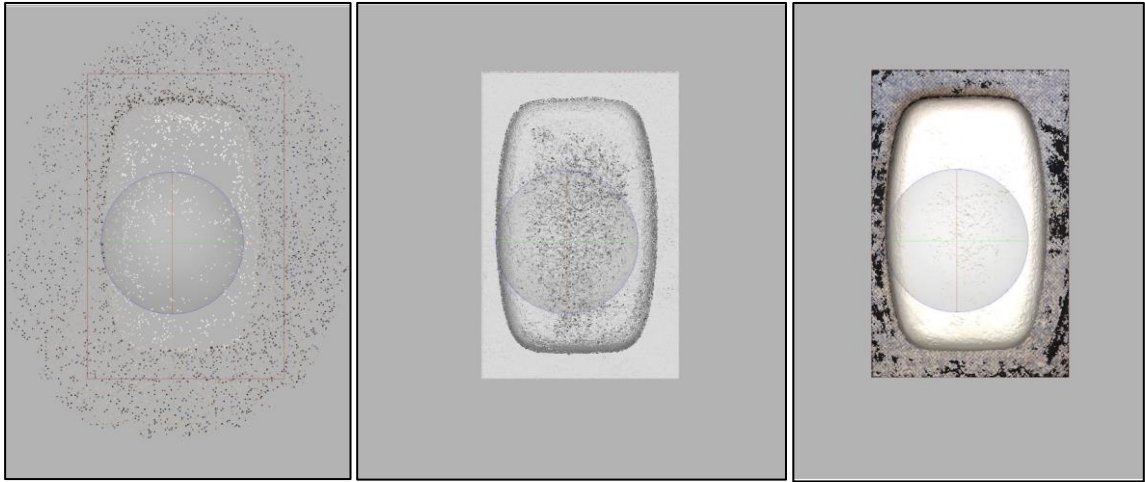


Illustration 25 Bounding box (in thin red) set close around the object

3.6 Agisoft Lens

The Agisoft PhotoScan comes with an add-on called Agisoft lens. Agisoft Lens is for pre-calibration of the lens used. A digital camera works by letting light pass through the lens and be projected onto the image sensor placed in the camera body. DSLR cameras allow for different lenses on a single body, allowing the photographer to change lens according to the scene. The quality, and subsequently the price of the lens are strongly related to the lens's ability to project the scene being photographed with as few optical errors as possible (Langford, Fox, & Smith, Langford's Advanced Photography, 2008). The distortions in the picture captured are mainly caused by the optical properties of the glass used in the lens and the accuracy of the build of both the lens and the camera components. The effect of these errors must be eliminated for accurate image coordinates to be obtained, and this process is the lens calibration. The lens calibration process is straightforward and easy to perform. First the SW shows a black and white chessboard pattern on the screen.

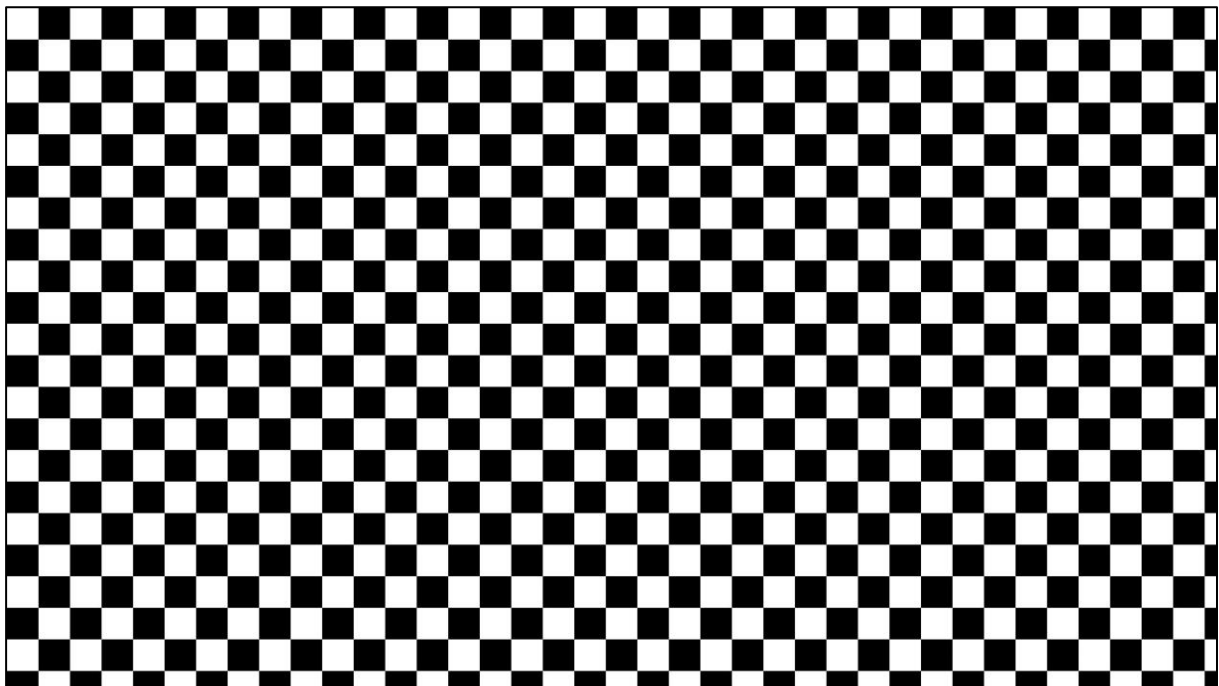


Illustration 26 Chess board pattern

A number of pictures (minimum 3 for any focal length) are taken of the screen at different angles. The pictures should only show the chessboard pattern, and nothing of the screen frame and surrounding area. The images are loaded into the Agisoft Lens Software, and the option to calibrate lens is chosen.

The following calibration parameters are estimated during calibration and printed in the Report window:

- fx - horizontal focal length, in pixels
- fy - vertical focal length, in pixels
- cx - X coordinate of the principal point
- cy - Y coordinate of the principal point
- K1, K2, K3, P1, P2 - radial lens distortions in the Brown's model((Agisoft LLC, 2011; Agisoft LLC, 2014)

The calibration result can be inspected visually for each photoset see illustration 27.

| Parameter | Value | Std Error |
|---------------------|--------------|-------------|
| Image width | 6016 | |
| Image height | 4000 | |
| Focal length (x) | 14750.8 | 6.54897 |
| Focal length (y) | 14752.1 | 6.01251 |
| Principal point (x) | 2958.52 | 9.66314 |
| Principal point (y) | 1985.73 | 6.8676 |
| Skew | 0 | 0 |
| Radial K1 | -0.164104 | 0.016021 |
| Radial K2 | 0.390697 | 0.671564 |
| Radial K3 | -7.85159 | 8.51353 |
| Radial K4 | 0 | 0 |
| Tangential P1 | 9.24239e-06 | 0.000115403 |
| Tangential P2 | -4.69694e-05 | 0.000138387 |

Illustration 27 Calibration Values

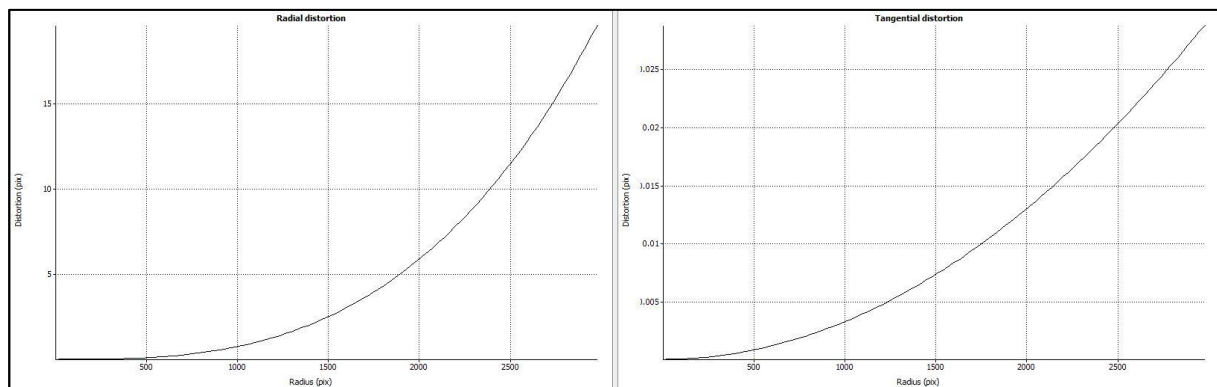


Illustration 28 Calibration result in graphic view

For the radial distortion the K1-K3 are expressed as units of focal length (F_x), so to get the convert them to pixels the values needs to be divided by $(F_x)^2$ for K1, $(F_x)^4$ for

K2 and $(F_x)^6$ for K3. The values achieved for the lens used in this experiment indicates very little distortion. The above calibration values were exported to an XML file that is compatible with Agisoft PhotoScan and imported as pre-calibration results. It has to be noted that the software does not give any indication of the quality of the calibration.

3.7 Workflow problems that were encountered and solved

3.7.1 Reversed z-axis

When building the model based on coordinates, there is a common problem that the model z value is reversed.

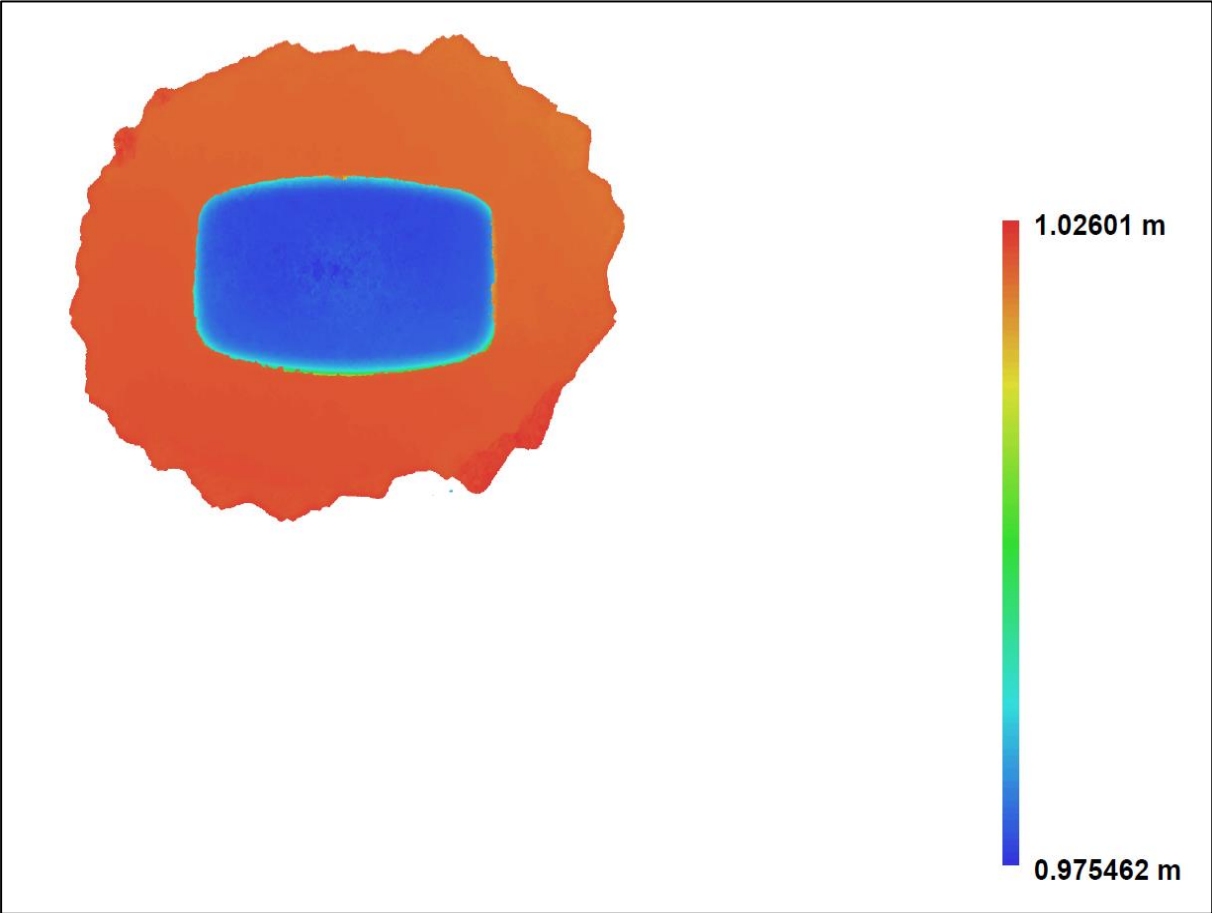


Illustration 29 DEM of reversed Z value, causing the floor to be ceiling

The problem is corrected by changing the x- and y-axis in the dataset. For this project, even the origin of the local coordinate system had to be recalculated. First it was set in the lower left-hand corner seen from photo number one but had to be recalculated to lower right-hand corner, and x- and y-axis changed for the correct axis alignment in PhotoScan.

3.7.2 Aligning of bounding box to model

The bounding box seems to be orientated at random when doing the photos alignment and it is the orientation of the bounding box that sets the orientation when exporting the model. To fix this problem a script in Python available on the PhotoScan wiki pages, the author not known. The script places a bounding box based on the axis coordinate system in use.

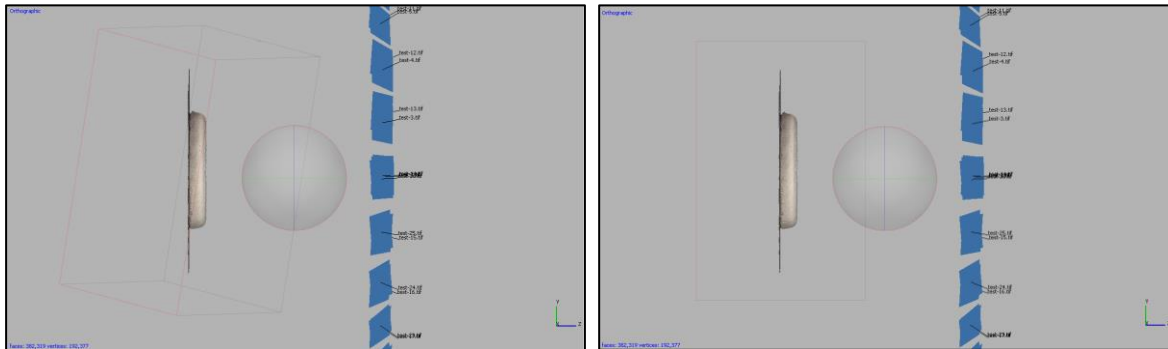


Illustration 30 Aligning bounding box

Before and after using a python script to align bounding box. Bounding box seen as thin red and grey lines. Red being box's ground plane

3.7.3 OpenCL

GPU aided proved to be difficult to enable. After not being able to utilize it on an ATI HD 6959 with a Cayman processor, the hardware was changed to an NVidia GTX 660 Ti. OpenCL went from not being enabled to showing the error "GPU processing failed, switching to CPU mode". Neither driver update nor reinstallation of PhotoScan helped. The problem with NVidia card proved to be program related, as update 1.1.3 had OpenCL enabled and working for the GTX 660 Ti.

3.8 MeshLab

In the early stages of this experiment, the need for an external mesh editor was clear the mesh editing in PhotoScan was resource demanding and was experienced to have poor performance. According to the software “MeshLab is an open source, portable, and extensible system for the processing and editing of unstructured 3D triangular meshes. The system is aimed to help the processing of the typical not-so-small unstructured models arising in 3D scanning, providing a set of tools for editing, cleaning, healing, inspecting, rendering and converting this kind of meshes” (Sourceforge.net). The reason for choosing Meshlab was this statement; “Currently there are thousands of users from all the world, coming from hundreds of universities and renowned commercial companies that have found MeshLab useful” (Cignoni, Corsini, & Ranzuglia, 2008). MeshLab performed well for the task at hand.

At the time, MeshLab proved to be less resource demanding than PhotoScan, and it also has functionality for volume measurement. In the beginning, MeshLab was the preferred tool for Volume estimation. As PhotoScan developed, MeshLab ended up as a verification of the mesh “close hole” and volume calculation.

The procedure is in short:

- export the 3-D model from PhotoScan using Stanford PLY format
- Remove any non-manifold edges, if needed, using the: Remove Faces from Non Manifold Edges filter
- Use Fill Hole option, setting Trivial
- Calculate mesh volume using Compute Geometric Measures filter

The Stanford format is chosen as it is also compatible with CloudCompare, and it is a standard format for 3-D models.

In MeshLab, there is a requirement that the model consist of only manifold edges before any mesh calculations can take place. So in the case that there are any non-manifold edges these are removed prior to filling holes and calculating volume. In illustration 31, next page, is from MeshLab, the bottom surface hole has been closed, and the resulting geometric calculations are displayed in the bottom right corner. For the setup used in this experiment, it was experienced that MeshLab was unstable, and would crash more often than any other software in use, for no apparent reason.

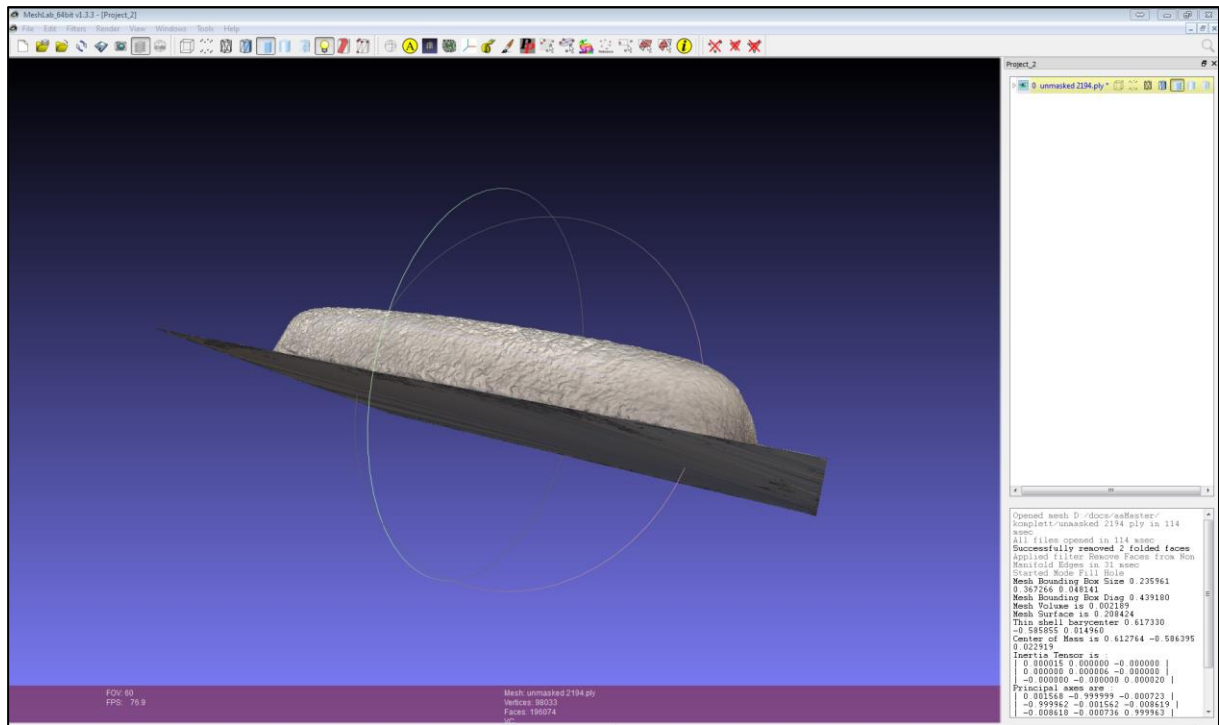


Illustration 31 Closed mesh in MeshLab

3.9 CloudCompare

CloudCompare is an Open source project that can be used for the cloud to cloud distance measurements. It has been widely used together with photogrammetry (Samaan, Héno, & Pierrot-Deseilligny, 2013) (Conte, 2014) for comparisons, mesh editing and distance calculations and verifications. Cloudcompare was used exclusively for the cloud to cloud distance comparison in this project. Moreover, any other possibility in the software was not explored.

The method is straightforward;

- The two clouds of interest are loaded into Cloudcompare using Stanford PLY format.
- The two clouds are aligned
- Distance between the two clouds is calculated

When aligning the two clouds, it was found that due to the small clouds and many faces, a high random sampling limit of 500000 was used.

When comparing the models, care should be taken to make sure the cloud being referenced to (in red) has a larger outreach than the cloud being compared to it (Yellow). Otherwise, there will be a statistical outlier on the edges, illustration 32 below.

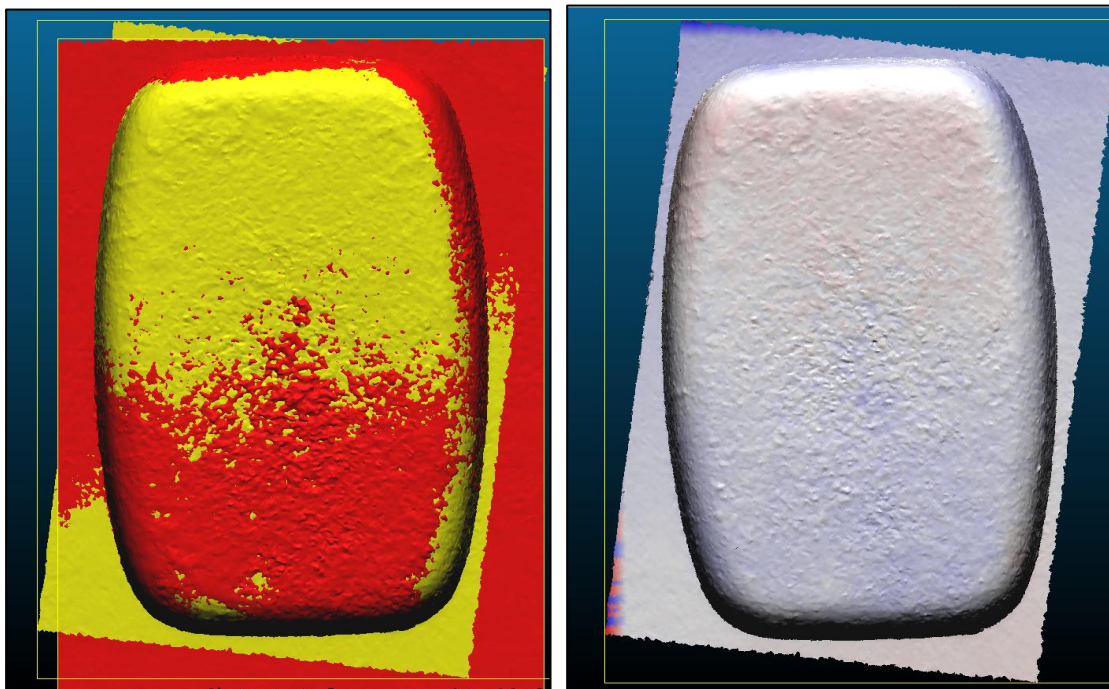


Illustration 32 Cloud comparison

The two small yellow parts outside the red model show as significant errors of several centimetres on the comparison plot (red and blue edge)

The differences are available as plots and graphs.

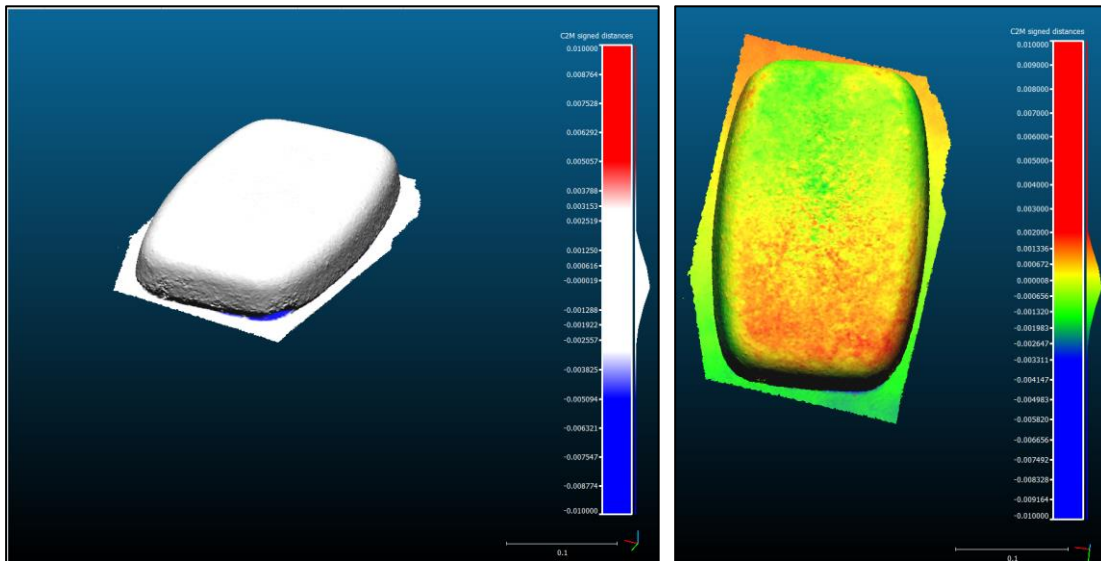


Illustration 33 Difference plot

Measurements in meters, colour scale ± 1 cm, white is within ± 3 mm

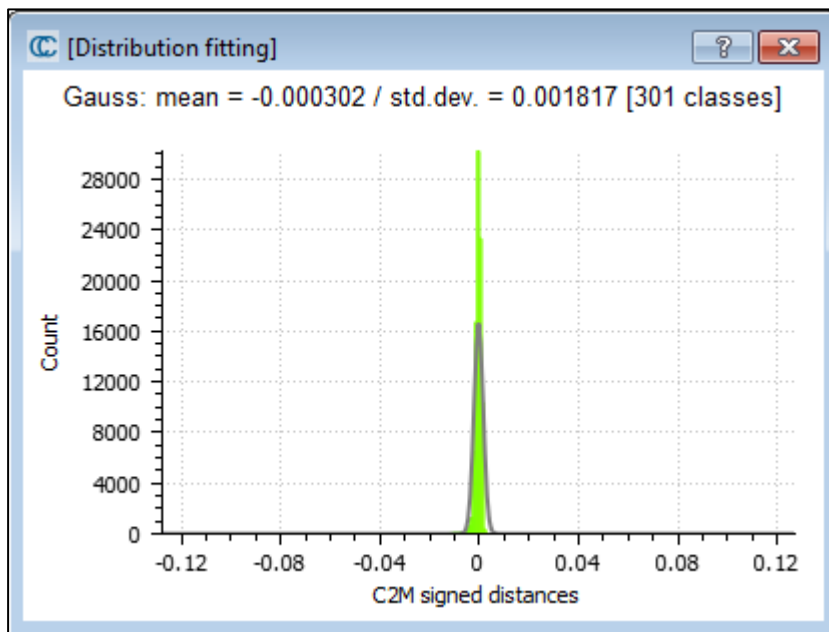


Illustration 34 Gauss distribution of comparison (in meters)

The mean is -0.3mm and the standard deviation is 2 mm

4 Marine ice accretion

4.1 Types of ice accretion

The liquid particles causing ice accretion is typically divided into two categories, atmospheric processes or windborne. The resulting ice is for windborne called rime or glaze, and for atmospheric frost, rime or glaze ice. Frost or “Hoarfrost” ice is caused by water vapour sublimating on a sub-zero surface. Frost is ice crystals directly formed from vapour and need a windless environment to form. (Ryerson C. C., 2011)

Rime ice is super-cooled water droplets that strike a freezing surface, causing the drops to freezing; wind normally carries them. Glaze or clear ice is precipitation striking a surface and have time to flow over the surface prior to freezing, creating a continuous film, normally a hard nearly homogenous ice that is as good as bubble-free. Sea spray is windborne particles, and according to Ryerson (2011) most investigators agree that sea spray is the greatest threat to offshore installations and vessels. It can be divided into two categories.

- The spray caused by wind alone, affecting stationary installations like platforms and quayside equipment and
- The spray formed by the splashing of waves towards a moving object in the sea (like a ship).

The latter is the greatest concern and has caused the most severe accidents, event sinking vessels. Seaspray does not normally extend more than 15 m above peak water level, and will pose little threat to large installation above this height (Ibid). Above this height, the precipitation and atmospheric icing are the most likely source of icing, often in combination (Ibid).

4.2 Conditions for ice accretion

According to the Norwegian meteorological institute (Tangen, 2014) the critical range for icing is air temperatures from -18°C to 0°C . Temperatures below -18°C will generally result in dry ice crystals that don't adhere to objects. Wind speeds above 9 m/s and sea temperatures between -2.2°C and 5°C are also a prerequisite. Sea temperatures below -2.2°C will typically freeze the ocean-surface and have a damping effect on all motion in the sea and minimize or remove the sea spray. Severe icing normally occurs at less maximum -5°C air and 3°C sea temperatures. For sea spray icing, the wind direction and speed relative to the vessel, the vessel size and the wave height all affect the total amount of spray and icing. In lieu of the above, it is clear that the most common period of icing is in the wintertime, for the Barents Sea this extends from October to April. For Longyearbyen at 78°N , the polar night extends from 26th October to 16th February, at which time there is no daylight. For the method proposed there will be a need for external light sources to accomplish photographs that can be processed in PhotoScan.

4.3 Effects of icing

The most severe effect of icing is the immediate loss of stability that can cause the vessel to capsize. This has occurred on several occasions, especially on small and medium sized fishing vessels (Zakrzewski, 1987). These vessels are more likely to be exposed to icing, and at the same time relatively less icing is required to destabilize the vessel. For oil rigs, there have been no occurrences where icing has been recorded as the cause of loss. There have been rigs lost in bad weather, but there is no indication that icing has contributed to these incidents. There have been recorded incidents with icing in the range between 225-450 Metric Ton on rigs in the North Sea (Ryerson C. C., 2011).

Icing can cause equipment to be frozen in solid ice, rendering the equipment useless; this is particularly serious if the windlass, survival-, positioning- or safety gear is affected. Blocking of ventilation and escape routes can pose a serious threat in combination with other events, but alone they are more of a nuisance. Icing on walkways, stairs and slipways are trip hazards and pose a threat at the individual level, but not so for the vessel. From my experience, icing of windows on the bridge of the vessel posed a serious threat to the vessel navigation. It was a hindrance to proper lookout and forced the vessel to rely on blind navigation alone. Extreme cold and snow pose a greater hazard to permanent offshore installations in the high north than sea spray, and de-icing measures will demand higher energy levels in high winds and low temperatures.

5 Results and discussion

In this chapter, the results of the experiment will be presented, along with a discussion of the main aspects around these.

5.1 CloudCompare

The cloud comparison showed that the surface of the model the difference between the rubber coated and the ice was all within $\pm 3\text{mm}$. For the small indent between the ice and the ground, the difference is slightly higher, but still within $\pm 5\text{mm}$ illustration 36, next page.

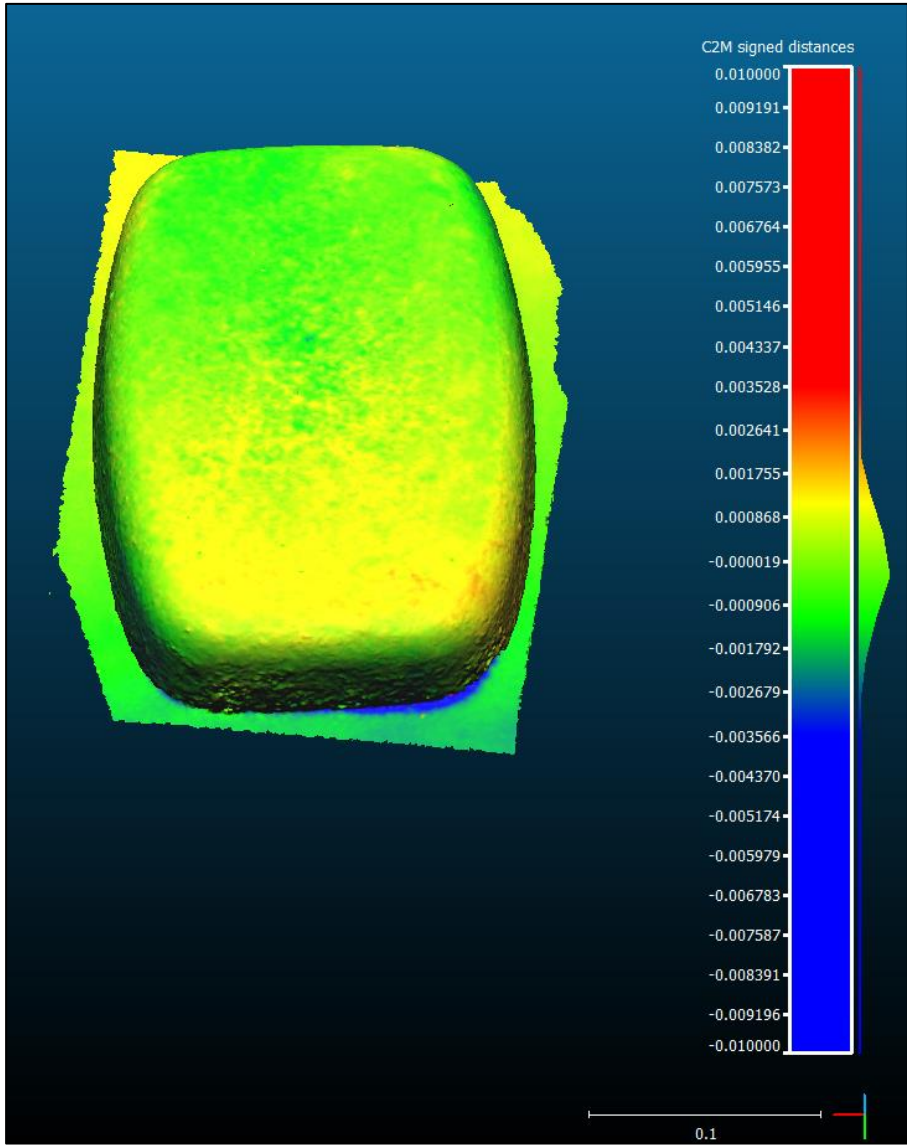


Illustration 35 Comparison plot, all within 3 mm

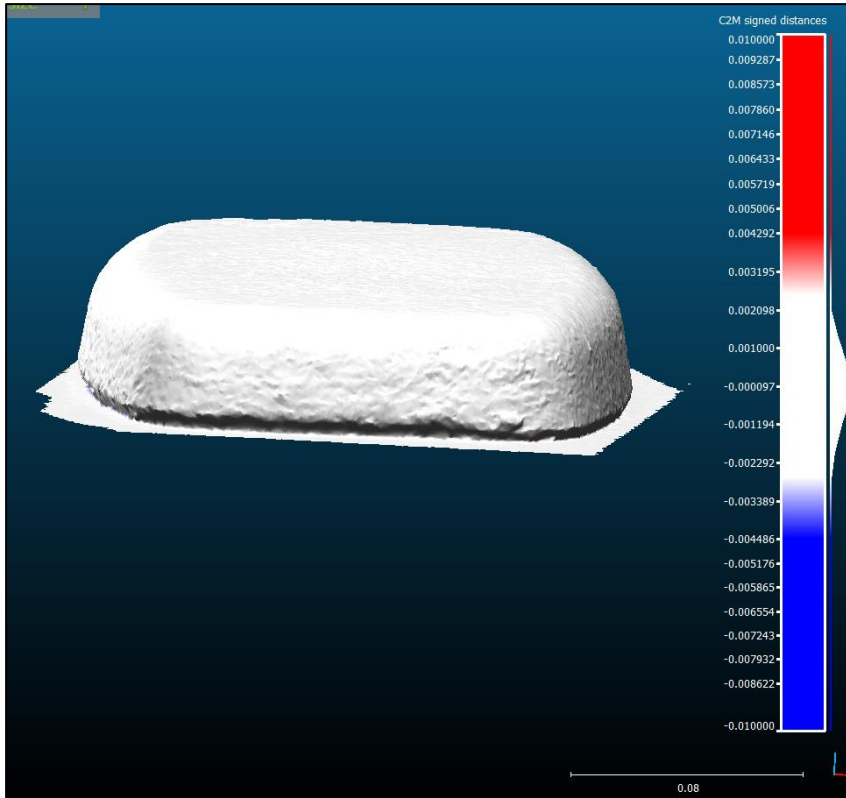


Illustration 36 Colouring starts at ± 4.5 mm.

5.2 Ice volume measurements

For the ice volume measurements, the following results were computed based on the digital models.

| Object | volume measured in | |
|--|--------------------|---------|
| | PhotoScan | MeshLab |
| Model of ice | 2191 ml | 2192 ml |
| Model of ice with mask on surroundings | 2194 ml | 2195 ml |
| Model of Blue rubber coated ice | 2185 ml | 2186 ml |

| Method | Volume cylinder | Density | Volume |
|------------------------|-----------------|---------|---------|
| Filling water | 163 ml | 0.877 | 2182 ml |
| Measured with calliper | 162.7 ml | 0.879 | 2177 ml |

Table 2 Ice model volume results

The ice frozen in the cylinder weighted 143 grams.

For the masked model, the error is in the region of 0.8% of the calculated volume based on the calliper measurements.

5.3 3-D Model Construction time

The 3-D model construction time was as follows:

- Photos Alignment 1-2 minutes
- Dense cloud construction 1-2 minute
- Mesh building 2-4 minutes

This adds to a total of 4-10 minutes processing time for 3-D model construction.

5.4 Discussion

The method proposed in this experiment has shown promising results, but there are still several issues to be resolved prior to a full-scale launch of a vessel or installation. The ice mesh data looks smooth without discrepancies, and the volumes differ with less than 10 ml for the three models that were processed and calculated. It should be noted that the workflow proposed for PhotoScan was the one experienced to give the best result for all three models and best repeatability. Even small changes in the workflow yielded slightly different results. From version 1.1.1 released in January 2015, the software is also capable of creating a mesh of the ice without camera positioning data. This mesh would, of course, be without any scale and orientation, but this could be solved by adding GCP's. Even older photosets shot at the beginning of this project, which proved impossible to align without camera positions were aligned in the latest version of PhotoScan. This implies that at the beginning of the experiment, the SFM algorithm was not ready to produce results as they are at later versions. Moreover, that the idea of using close range photogrammetry was premature for this particular software at the time.

The camera used had problems focusing on the ice; even the lighting was sufficient. A camera with better autofocus would be preferred if this were to be a full-scale system. To avoid this problem, the focus could be pre-set to a certain distance. Providing the DOF is wide enough, and that the area of interest is in focus, the images should be sharp. The drawback with this approach is if parts of the area of interest are outside the focused area, it would never appear sharp. In 2012, the first consumer grade light field camera, the Lytro, was available (Georgieva, Yub, Lumsdaine, & Goma, 2013). A light field, also known as plenoptic camera can focus after the image is shot. The user can change the focus area in the picture in post-processing, a "digital lens". In theory, this would correct one of the crucial points in close range photogrammetry of ice. There is no documentation of compatibility for this type of camera in PhotoScan, but the technique is eliminating a significant source of concern but needs to be tested before any conclusion is made.

The quality of the photos used for the ice model are all rated to be below the criteria (0.5) set by PhotoScan. This experiment has shown that that models created even with substandard quality is capable of producing accurate 3-D models. However, the result could in this particular experiment have gained in the fact that the ice had few

features. There is little doubt that the possibility for the biggest improvement in this experiment is better quality photos, with higher DOF. The lack of depth in the pictures is also visible, and it is strongly believed that a better composition of the scene will result in more DOF and better photogrammetry quality in the photos.

The accuracy of the models is also within the expected accuracy for close range photogrammetry.

The edge dip on the 3-D models for the calculations without mask proved to have little impact on the volume, as long as the bounding box was set to be inside the dip. For the masked model, there is no clear limit between the ice and the ground, and it was very difficult to determine where the ground plane was. In lieu of this it is recommended to extend the model bounding box to allow for the ground to be clearly visible prior to closing holes. The resulting volume calculations will be more accurate and comparable, as long as the bounding box does not include any edge dip.

For the weight used the accuracy is 1 gram and a worst case scenario where the error is unevenly distributed, the density of the extracted ice can vary from 0.866(142/164) to 0.889 (144/162) resulting in a volume of 2152ml - 2210ml. The resulting error is still less than 2%. This is the worst case, and there is no indication that there was any bias error in the weight measurements of the ice. The density is identified as the single calculation in this experiment that leads to largest error in the result.

In a full-scale scenario, the density of the ice would normally be unknown, and there are several challenges in accurate measurements of the ice density (G.W. Timco, 1996). Typically the density will vary between 0.72 kg/T to 0.94 kg/T (Ibid). An attempt at the mentioned displacement technique proposed in the "A review of sea ice density" was tested in this experiment; beforehand the ice had been vacuum sealed in a plastic bag. However, as the ice was submerged into the cold water the outer layer of the ice froze the water, and it ended up with an approximate 10% added volume after being submerged in 10 seconds. Needless to say, this method of calculating the density was abandoned, but it is worth mentioning that the problem experienced with this technique was not mentioned in the paper. Since the ice had been vacuumed, it was unproblematic to remove the excess ice. The uncertainty of the ice density could in an operative environment prove to be a larger source of error than that of the model of the ice. This providing the photogrammetry accuracy of

larger ice volumes has the same accuracy as in this experiment. The use of MeshLab has, with the advances in PhotoScan, become superfluous and can be removed from the workflow, the volume calculation and mesh editing tools in PhotoScan will be sufficient.

It is evident that CloudCompare also can be used in ice rate estimation, comparing mesh clouds created at different time intervals. The highest, lowest and average icing rate will be easy accessible, and clearly visible on a 3-D model of the difference between 2 clouds. By utilizing this there is no need to introduce foreign objects to measure icing on, and the results could prove valuable and accurate for the particular installation or vessel.

The setup in this experiment, with only camera positions and no scale bar or GCP's, was to prove that ice can be modelled in PhotoScan. In a future development of this method, it would be natural to include both scale bars and GCP's to improve the accuracy of the model. Scale bars could be set by introducing parallel laser beams with known distance between two laser light. Markers used to define the endpoints on the pictures prior to alignment could easily give size to the cloud. The procedure is straightforward and easy to apply.

The total time used to create a mesh was less than 10 minutes, and that is well within an acceptable timeframe for a ship or platform official to make adequate decisions regarding ice accretion. The time can be reduced with newer and faster equipment, but that will, of course, come with a price penalty.

For a full-scale deployment, the biggest issue is how to get the camera in positions that can circumference the area of interest. On a vessel, the area that is most affected of sea spray icing is the bow, and it could prove difficult to get pictures around this area. A proposal is UAV mounted camera, but that might prove difficult in harsh weather conditions. On a newly built vessel, a camera system could be designed in as a feature in the early stages, avoiding having to accommodate for this after the vessel is built.

The fact that the PhotoScan software is capable of modelling objects that have key properties that are specified as "to be avoided" can open new dimensions for the application. For instance could ice-cave documentation be one area of interest, snow detection and volume estimation for accurate avalanche forecasting another.

5.5 Conclusion

This experiment has shown that ice volume measurements are possible using close range photogrammetry as a method. The volume calculation of the mesh is within more than 99.2% of that of the actual ice block. Moreover, all volume calculations have been verified by two different software packages. The density calculations are based on two different methods of verifying the ice volume, calliper measurements and water weight. All weighting has been repeated three times with no discrepancy in the measurements. Over the duration of the experiment, it has become clear that advances in the PhotoScan software have had a crucial impact on the result.

The experiment has proven that it is unproblematic to remote control and remote storage of data in real time with a consumer grade camera. The only requirement is the availability of a wireless network. The software used is also capable of processing a mesh within an acceptable time to make real-time decisions, and there is room for improvement using newer, state of the art computation hardware.

6 Future work

6.1.1 Full-scale testing

The methodology has proven satisfactory results in a controlled environment, but it needs to be tested in a real marine icing environment to prove that it can handle larger volumes and outdoor conditions.

6.1.2 Camera operations in sub-zero temperatures

The camera used in this experiment is not rated for use in sub-zero temperatures. After checking the other major manufacturer's equipment specifications the consumer grade DSLR cameras have an operating environment of 0°-40°C in less than 85% humidity (no condensation). Even the "freeze proof" Nikon 1 AW1 camera is only rated down to -10°C (Nikon, 2014).

It is common knowledge that most of the amateur Aurora-borealis photographers in the Arctic region of Norway, Sweden and Finland use Consumer-grade cameras. The pictures taken outdoors in January and February are often taken in as low as -15C and colder. From discussions with experienced expert Aurora photographers I have been told that the most common problem is shortened battery life, and in extreme cold the autofocus can be experienced to performs slowly and inaccurate. However, for night sky pictures the autofocus is not used, and the accuracy of the geometry is of no importance.

To be able to use a consumer grade DSLR for ice accretion estimation, the camera and lens performance will have to be tested and verified.

6.1.3 Camera positioning

Accurate positioning of the camera in a live environment is necessary for PhotoScan to create a measurable cloud, if not the cloud will have no scale or size. Equipment to precisely position the camera is needed, unless there are readily available GCP, then the SFM positions can be sufficient.

6.1.4 File formats and post processing

In this experiment, the photos were not post-processed prior to importing them in PhotoScan. The result of the experiment was deemed adequate, but it would prove beneficial to know if post processing can improve the results. If so, automating post-processing will likely not introduce any time delay into the process, but if it has to be manual labour a time versus improvement achieved analysis is needed.

6.1.5 QDslrDashboard PC version

The qDslrDashboard latest edition also comes with a Windows PC application. In conjunction with a PC running PhotoScan, this allows for instant loading of pictures into PhotoScan to determine if two pictures have enough common points to be accepted, or if one or both have to be reacquired. This can streamline the acquisition even more, and eliminate the Android device used in this experiment.

6.1.6 Active use of Light to identify ice

For the application of photogrammetry on marine ice accretion in the Arctic region, there will be prolonged periods of time where the images have to be shot when darkness prevails. To overcome this use of external light sources will be necessary, but this also presents an opportunity to project a unique light pattern onto the ice surface for better performance in PhotoScan.

6.1.7 Review of Lytro camera

A review of the Lytro camera compatibility with PhotoScan, and assessment of close range photogrammetry capabilities is necessary. This can prove whether this is a way forward or a dead end.

6.1.8 Higher quality settings in building dense cloud

It would be interesting to know if increasing the quality of the dense cloud can improve the accuracy of the mesh, and if the increase in processing time this causes can be justified by more accurate cloud data. Also investigations into the performance increase of other GPU's and now also the network capability of

PhotoScan to minimize processing time and maximising accuracy could prove valuable for budgeting and processing flow.

6.1.9 Automation of workflow

PhotoScan supports Python scripting and could allow for automation of the steps used in the described workflow.

7 Bibliography

- Agisoft LLC. (2011). *Agisoft lens user manual* . Retrieved from Agisoft downloads:
<http://downloads.agisoft.ru/lens/doc/en/lens.pdf>
- Agisoft LLC. (2014). *Agisoft PhotoScan user manual*. Retrieved from Agisoft
downloads: http://www.agisoft.com/pdf/photoscan-pro_1_1_en.pdf
- Agisoft LLC. (2015, 02 27). *Agisoft PhotoScan Change Log*. Retrieved from Agisoft
Downloads: http://downloads.agisoft.ru/pdf/photoscan_changelog.pdf
- Cignoni, P., Corsini, M., & Ranzuglia, G. (2008). Meshlab: an open-source 3d mesh
processing system. *Ercim news*(73), pp. 45-46.
- Collier, P. D. (1999). The use of close range photogrammetry for studying ice
accretion on aerofoil sections. *The Photogrammetric Record*, 671-684.
- Conte, G. P. (2014). Evaluation of a light-weight LiDAR and a photogrammetric
system for unmanned airborne mapping applications. *Photogrammetrie-
Fernerkundung-Geoinformation*, 287-298.
- Faglig Forum. (2010). *Det faglige grunnlaget for oppdateringen av forvaltningsplanen
for Barentshavet og havområdene utenfor Lofoten 2010*. Bergen:
Havforskningsinstituttet.
- G.W. Timco, R. F. (1996). A review of sea ice density. *Cold Regions Science and
Technology*, 24(1), 1-6. doi:10.1016/0165-232X(95)00007-X
- Georgieva, T., Yub, Z., Lumsdaine, A., & Gomaa, S. (2013). Lytro camera
technology: theory, algorithms, performance analysis. *Proc. SPIE 8667,
Multimedia Content and Mobile Devices*. Burlingame: SPIE.
doi:10.1117/12.2013581
- Guy, G., Marc, R., J.-Angelo, B., Marc, L., Luc, C., & Godin, G. (2001). An
assessment of Laser range measurement on marble surfaces. (p. Optical 3D
measurement techniques). Vienna: Stanford edu.
- J. E. Overland, C. H. (1986). Prediction of vessel icing. *J. Climate Appl. Meteor*,
1793-1806. doi:10.1175/1520-0450(1986)025<1793:POVI>2.0.CO;2
- Langford, M., Fox, A., & Smith, R. S. (2007). *Langford's Basic Photography* (8 ed.).
Burlington: Focal Press.
- Langford, M., Fox, A., & Smith, R. S. (2008). *Langford's Advanced Photography* (7
ed.). Burlington: Focal Press.

- Luhmann, T., Robson, S., Kyle, S., & Harley, I. (2011). *Close Range Photogrammetry Principles, techniques and applications*. Dunbeath: Whittles Publishing.
- M.J. Westoby, J. B. (2012, 12 15). 'Structure-from-Motion' photogrammetry: A low-cost, effective tool for geoscience applications. *Geomorphology*, 179, 300-314. doi:10.1016/j.geomorph.2012.08.021
- Nikon. (2014). <http://imaging.nikon.com>. Retrieved from <http://imaging.nikon.com>: <http://imaging.nikon.com/lineup/acil/bodies/aw1/spec.htm>
- Perovich, D. K. (2003, October). Complex yet translucent: the optical properties of sea ice. *Conference on Electrical Transport and Optical Properties of Inhomogeneous Media* (pp. 107-114). Snowbird, UT, USA: Elsevier B.V. doi:10.1016/S0921-4526(03)00470-8
- Ryerson, C. C. (2009). *Assessment of superstructure ice protection as applied to offshore oil operations safety*.
- Ryerson, C. C. (2011). Ice protection of offshore platforms. *Cold Regions Science and Technology*, 65(1), 97-110. doi:10.1016/j.coldregions.2010.02.006.
- Samaan, M., Héno, R., & Pierrot-Deseilligny, M. (2013). Close-range photogrammetric tools for small 3D archeological objects. *XXIV International CIPA Symposium*. Strasbourg.
- Semyonov, D. (2011, 05 03). *Agisoft community forum*. Retrieved from Topic: Algorithms used in Photoscan: <http://www.agisoft.com/forum/index.php?topic=89.0>
- Sourceforge.net. (n.d.). *Meshlab*. Retrieved from Meshlab: <http://meshlab.sourceforge.net/>
- Tangen, H. (2014, 05 20). *Norsk olje og gass*. Retrieved from https://www.norskoljeoggass.no/Global/HMS-utfordringer%20i%20nordomr%C3%A5dene/Seminar%204%20-%20Risikostyring%20og%20design/0915%20Tangen%20Arbeidsseminar_4_Tangen_2014_V1.0.pdf
- Verhoeven, G. (2011, 1 20). Taking computer vision aloft – archaeological three-dimensional reconstructions from aerial photographs with photoscan. *Archaeological Prospection*, pp. 67-73. doi:10.1002/arp.399

Zakrzewski, W. (1987). Splashing a ship with collision-generated spray. *Cold Regions Science and Technology*, 14(1), 65-83. doi:10.1016/0165-232X(87)90045-0

8 Table of figures

| | |
|--|----|
| Illustration 1 Rotation of polarized light emitted by sensors show the presence of ice or snow | 4 |
| Illustration 2 Vaisala road ice detector | 6 |
| Illustration 3 Pole ice with ice accretion..... | 7 |
| Illustration 4 Photogrammetry model..... | 11 |
| Illustration 5 Marine ice accretion | 15 |
| Illustration 6 Camera setup around the ice | 18 |
| Illustration 7 Correct camera setup for isolated object | 19 |
| Illustration 8 Images used for comparison of image quality | 19 |
| Illustration 9 Depth of Field..... | 22 |
| Illustration 10 DOF at 0.5 m f-stop f/2.8 | 23 |
| Illustration 11 Aperture | 24 |
| Illustration 12 Blitz used in snowfall | 25 |
| Illustration 13 Image quality estimation | 29 |
| Illustration 14 Lens calibration values applied..... | 30 |
| Illustration 15 Picture with the mask applied..... | 31 |
| Illustration 16 Mask file | 31 |
| Illustration 17 Sparse point cloud | 32 |
| Illustration 18 Camera estimated errors..... | 33 |
| Illustration 19 Feature point matches with masks enabled | 34 |
| Illustration 20 Feature point matches without masks enabled | 34 |
| Illustration 21 Mesh..... | 36 |
| Illustration 22 3-D model of ice | 37 |
| Illustration 23 Slight dip at the edge of the model | 37 |
| Illustration 24 Before and after cropping the model | 38 |
| Illustration 25 Bounding box (in thin red) set close around the object | 38 |
| Illustration 26 Chess board pattern..... | 39 |
| Illustration 27 Calibration Values | 40 |
| Illustration 28 Calibration result in graphic view | 40 |
| Illustration 29 DEM of reversed Z value, causing the floor to be ceiling..... | 42 |
| Illustration 30 Aligning bounding box..... | 43 |
| Illustration 31 Closed mesh in MeshLab | 45 |
| Illustration 32 Cloud comparison..... | 46 |
| Illustration 33 Difference plot | 47 |
| Illustration 34 Gauss distribution of comparison (in meters)..... | 47 |
| Illustration 35 Comparison plot, all within 3 mm | 53 |
| Illustration 36 Colouring starts at ± 4.5 mm. | 54 |

9 Appendix

9.1 Appendix 1: Exif data

| DerivedFrom | |
|--------------------------|------------------------|
| ApertureValue | 1695994/1000000 |
| CFAPattern | 2, 0, 2, 0, 0, 1, 1, 2 |
| Contrast | 0 |
| CustomRendered | 0 |
| DateTime | 2015:04:20 14:19:00 |
| DateTimeDigitized | 2015:03:23 14:40:07 |
| DateTimeOriginal | 2015:03:23 14:40:07 |
| DigitalZoomRatio | 1/1 |
| ExifOffset | 216 |
| ExifVersion | 48, 50, 51, 48 |
| ExposureBiasValue | 0/6 |
| ExposureMode | 0 |
| ExposureProgram | 0 |
| ExposureTime | 1/60 |
| FileSource | 3 |
| Flash | 16 |
| FNumber | 18/10 |
| FocalLength | 500/10 |
| FocalLengthIn35mmFilm | 75 |
| FocalPlaneResolutionUnit | 4 |
| FocalPlaneXResolution | 8504122/32768 |
| FocalPlaneYResolution | 8504122/32768 |
| GainControl | 2 |
| ISOSpeedRatings | 900 |
| LightSource | 0 |
| Make | NIKON CORPORATION |
| MaxApertureValue | 16/10 |
| MeteringMode | 5 |

| | |
|----------------------|---|
| Model | NIKON D3200 |
| ResolutionUnit | 2 |
| Saturation | 0 |
| SceneCaptureType | 0 |
| SceneType | 1 |
| SensingMethod | 2 |
| Sharpness | 0 |
| ShutterSpeedValue | 5906891/1000000 |
| Software | Adobe Photoshop Lightroom 4.4 (Windows) |
| SubjectDistanceRange | 0 |
| SubSecTimeDigitized | 50 |
| SubSecTimeOriginal | 50 |
| WhiteBalance | 0 |
| XResolution | 240/1 |
| YResolution | 240/1 |
| colorspace | 2 |
| ApertureValue | 1695994/1000000 |
| CFAPattern | 2, 0, 2, 0, 0, 1, 1, 2 |
| Contrast | 0 |
| CustomRendered | 0 |
| DateTime | 2015:04:20 14:19:00 |
| DateTimeDigitized | 2015:03:23 14:40:07 |
| DateTimeOriginal | 2015:03:23 14:40:07 |
| DigitalZoomRatio | 1/1 |
| ExifOffset | 216 |
| ExifVersion | 48, 50, 51, 48 |
| ExposureBiasValue | 0/6 |
| ExposureMode | 0 |
| ExposureProgram | 0 |
| ExposureTime | 1/60 |
| FileSource | 3 |
| Flash | 16 |

| | |
|--------------------------|---|
| FNumber | 18/10 |
| FocalLength | 500/10 |
| FocalLengthIn35mmFilm | 75 |
| FocalPlaneResolutionUnit | 4 |
| FocalPlaneXResolution | 8504122/32768 |
| FocalPlaneYResolution | 8504122/32768 |
| GainControl | 2 |
| ISOSpeedRatings | 900 |
| LightSource | 0 |
| Make | NIKON CORPORATION |
| MaxApertureValue | 16/10 |
| MeteringMode | 5 |
| Model | NIKON D3200 |
| ResolutionUnit | 2 |
| Saturation | 0 |
| SceneCaptureType | 0 |
| SceneType | 1 |
| SensingMethod | 2 |
| Sharpness | 0 |
| ShutterSpeedValue | 5906891/1000000 |
| Software | Adobe Photoshop Lightroom 4.4 (Windows) |
| SubjectDistanceRange | 0 |
| SubSecTimeDigitized | 50 |
| SubSecTimeOriginal | 50 |
| WhiteBalance | 0 |
| XResolution | 240/1 |
| YResolution | 240/1 |
| sampling-factor | 2x2,1x1,1x1 |
| ApertureValue | 1695994/1000000 |
| CFAPattern | 2, 0, 2, 0, 0, 1, 1, 2 |
| Contrast | 0 |
| CustomRendered | 0 |

| | |
|--------------------------|---------------------|
| DateTime | 2015:04:20 14:19:00 |
| DateTimeDigitized | 2015:03:23 14:40:07 |
| DateTimeOriginal | 2015:03:23 14:40:07 |
| DigitalZoomRatio | 1/1 |
| ExifOffset | 216 |
| ExifVersion | 48, 50, 51, 48 |
| ExposureBiasValue | 0/6 |
| ExposureMode | 0 |
| ExposureProgram | 0 |
| ExposureTime | 1/60 |
| FileSource | 3 |
| Flash | 16 |
| FNumber | 18/10 |
| FocalLength | 500/10 |
| FocalLengthIn35mmFilm | 75 |
| FocalPlaneResolutionUnit | 4 |
| FocalPlaneXResolution | 8504122/32768 |
| FocalPlaneYResolution | 8504122/32768 |
| GainControl | 2 |
| ISOSpeedRatings | 900 |
| LightSource | 0 |
| Make | NIKON CORPORATION |
| MaxApertureValue | 16/10 |
| MeteringMode | 5 |
| Model | NIKON D3200 |
| ResolutionUnit | 2 |
| Saturation | 0 |
| SceneCaptureType | 0 |
| SceneType | 1 |
| SensingMethod | 2 |
| Sharpness | 0 |
| ShutterSpeedValue | 5906891/1000000 |

| | |
|--------------------------|---|
| Software | Adobe Photoshop Lightroom 4.4 (Windows) |
| SubjectDistanceRange | 0 |
| SubSecTimeDigitized | 50 |
| SubSecTimeOriginal | 50 |
| WhiteBalance | 0 |
| XResolution | 240/1 |
| YResolution | 240/1 |
| modify | 2015-04-20T05:29:32-07:00 |
| ApertureValue | 1695994/1000000 |
| CFAPattern | 2, 0, 2, 0, 0, 1, 1, 2 |
| Contrast | 0 |
| CustomRendered | 0 |
| DateTime | 2015:04:20 14:19:00 |
| DateTimeDigitized | 2015:03:23 14:40:07 |
| DateTimeOriginal | 2015:03:23 14:40:07 |
| DigitalZoomRatio | 1/1 |
| ExifOffset | 216 |
| ExifVersion | 48, 50, 51, 48 |
| ExposureBiasValue | 0/6 |
| ExposureMode | 0 |
| ExposureProgram | 0 |
| ExposureTime | 1/60 |
| FileSource | 3 |
| Flash | 16 |
| FNumber | 18/10 |
| FocalLength | 500/10 |
| FocalLengthIn35mmFilm | 75 |
| FocalPlaneResolutionUnit | 4 |
| FocalPlaneXResolution | 8504122/32768 |
| FocalPlaneYResolution | 8504122/32768 |
| GainControl | 2 |
| ISOSpeedRatings | 900 |

| | |
|----------------------|---|
| LightSource | 0 |
| Make | NIKON CORPORATION |
| MaxApertureValue | 16/10 |
| MeteringMode | 5 |
| Model | NIKON D3200 |
| ResolutionUnit | 2 |
| Saturation | 0 |
| SceneCaptureType | 0 |
| SceneType | 1 |
| SensingMethod | 2 |
| Sharpness | 0 |
| ShutterSpeedValue | 5906891/1000000 |
| Software | Adobe Photoshop Lightroom 4.4 (Windows) |
| SubjectDistanceRange | 0 |
| SubSecTimeDigitized | 50 |
| SubSecTimeOriginal | 50 |
| WhiteBalance | 0 |
| XResolution | 240/1 |
| YResolution | 240/1 |
| create | 2015-04-20T05:29:32-07:00 |
| ApertureValue | 1695994/1000000 |
| CFAPattern | 2, 0, 2, 0, 0, 1, 1, 2 |
| Contrast | 0 |
| CustomRendered | 0 |
| DateTime | 2015:04:20 14:19:00 |
| DateTimeDigitized | 2015:03:23 14:40:07 |
| DateTimeOriginal | 2015:03:23 14:40:07 |
| DigitalZoomRatio | 1/1 |
| ExifOffset | 216 |
| ExifVersion | 48, 50, 51, 48 |
| ExposureBiasValue | 0/6 |
| ExposureMode | 0 |

| | |
|--------------------------|---|
| ExposureProgram | 0 |
| ExposureTime | 1/60 |
| FileSource | 3 |
| Flash | 16 |
| FNumber | 18/10 |
| FocalLength | 500/10 |
| FocalLengthIn35mmFilm | 75 |
| FocalPlaneResolutionUnit | 4 |
| FocalPlaneXResolution | 8504122/32768 |
| FocalPlaneYResolution | 8504122/32768 |
| GainControl | 2 |
| ISOSpeedRatings | 900 |
| LightSource | 0 |
| Make | NIKON CORPORATION |
| MaxApertureValue | 16/10 |
| MeteringMode | 5 |
| Model | NIKON D3200 |
| ResolutionUnit | 2 |
| Saturation | 0 |
| SceneCaptureType | 0 |
| SceneType | 1 |
| SensingMethod | 2 |
| Sharpness | 0 |
| ShutterSpeedValue | 5906891/1000000 |
| Software | Adobe Photoshop Lightroom 4.4 (Windows) |
| SubjectDistanceRange | 0 |
| SubSecTimeDigitized | 50 |
| SubSecTimeOriginal | 50 |
| WhiteBalance | 0 |
| XResolution | 240/1 |
| YResolution | 240/1 |

9.2 Appendix 2: Camera positions for ice

9.2.1 Camera positions for ice

| | | | |
|-------------|------|-------|------|
| test-1.tif | 0.00 | -0.60 | 0.55 |
| test-2.tif | 0.00 | -0.60 | 0.55 |
| test-3.tif | 0.02 | -0.44 | 0.55 |
| test-4.tif | 0.08 | -0.30 | 0.55 |
| test-5.tif | 0.18 | -0.18 | 0.55 |
| test-6.tif | 0.30 | -0.08 | 0.55 |
| test-7.tif | 0.44 | -0.02 | 0.55 |
| test-8.tif | 0.60 | 0.00 | 0.55 |
| test-9.tif | 0.76 | -0.02 | 0.55 |
| test-10.tif | 0.90 | -0.08 | 0.55 |
| test-11.tif | 1.02 | -0.18 | 0.55 |
| test-12.tif | 1.12 | -0.30 | 0.55 |
| test-13.tif | 1.18 | -0.44 | 0.55 |
| test-14.tif | 1.20 | -0.60 | 0.55 |
| test-15.tif | 1.18 | -0.76 | 0.55 |
| test-16.tif | 1.12 | -0.90 | 0.55 |
| test-17.tif | 1.02 | -1.02 | 0.55 |
| test-18.tif | 0.90 | -1.12 | 0.55 |
| test-19.tif | 0.75 | -1.18 | 0.55 |
| test-20.tif | 0.60 | -1.20 | 0.55 |
| test-21.tif | 0.44 | -1.18 | 0.55 |
| test-22.tif | 0.30 | -1.12 | 0.55 |
| test-23.tif | 0.18 | -1.02 | 0.55 |
| test-24.tif | 0.08 | -0.90 | 0.55 |
| test-25.tif | 0.02 | -0.75 | 0.55 |
| test-26.tif | 0.02 | -0.60 | 0.55 |

9.2.2 Camera positions for rubber coated ice

| | | | |
|------------|------|-------|------|
| bla-1.tif | 0.01 | -0.61 | 0.55 |
| bla-2.tif | 0.02 | -0.46 | 0.55 |
| bla-3.tif | 0.08 | -0.31 | 0.55 |
| bla-4.tif | 0.18 | -0.19 | 0.55 |
| bla-5.tif | 0.29 | -0.10 | 0.55 |
| bla-6.tif | 0.44 | -0.04 | 0.55 |
| bla-7.tif | 0.59 | -0.02 | 0.55 |
| bla-8.tif | 0.74 | -0.04 | 0.55 |
| bla-9.tif | 0.88 | -0.09 | 0.55 |
| bla-10.tif | 1.01 | -0.18 | 0.55 |
| bla-11.tif | 1.10 | -0.29 | 0.55 |
| bla-12.tif | 1.17 | -0.45 | 0.55 |
| bla-13.tif | 1.18 | -0.60 | 0.55 |
| bla-14.tif | 1.16 | -0.76 | 0.55 |
| bla-15.tif | 1.09 | -0.90 | 0.55 |
| bla-16.tif | 1.00 | -1.02 | 0.55 |
| bla-17.tif | 0.88 | -1.12 | 0.55 |
| bla-18.tif | 0.73 | -1.17 | 0.55 |
| bla-19.tif | 0.58 | -1.19 | 0.55 |
| bla-20.tif | 0.44 | -1.15 | 0.55 |
| bla-21.tif | 0.31 | -1.09 | 0.55 |
| bla-22.tif | 0.20 | -0.99 | 0.55 |
| bla-23.tif | 0.11 | -0.88 | 0.55 |
| bla-24.tif | 0.05 | -0.75 | 0.55 |
| bla-25.tif | 0.03 | -0.60 | 0.55 |

9.3 Appendix 3: Python script for bounding box alignment

```
#rotates chunks' bounding box in accordance of coordinate system for active chunk
```

```
#bounding box size is kept
```

```
#compatibility: Agisoft PhotoScan Professional 1.1.0
```

```
import PhotoScan
```

```
import math
```

```
doc = PhotoScan.app.document
```

```
chunk = doc.chunk
```

```
T = chunk.transform.matrix
```

```
v_t = T * PhotoScan.Vector( [0,0,0,1] )
```

```
v_t.size = 3
```

```
if chunk.crs:
```

```
    m = chunk.crs.localframe(v_t)
```

```
else:
```

```
    m = PhotoScan.Matrix().diag([1,1,1,1])
```

```
m = m * T
```

```
s = math.sqrt(m[0,0] ** 2 + m[0,1] ** 2 + m[0,2] ** 2) #scale factor
```

```
R = PhotoScan.Matrix( [[m[0,0],m[0,1],m[0,2]], [m[1,0],m[1,1],m[1,2]],  
[m[2,0],m[2,1],m[2,2]]])
```

```
R = R * (1. / s)
```

```
reg = chunk.region
```

```
reg.rot = R.t()
```

```
chunk.region = reg
```

9.4 Appendix 4: PhotoScan processing reports

Agisoft PhotoScan

Processing Report
24 April 2015



Survey Data

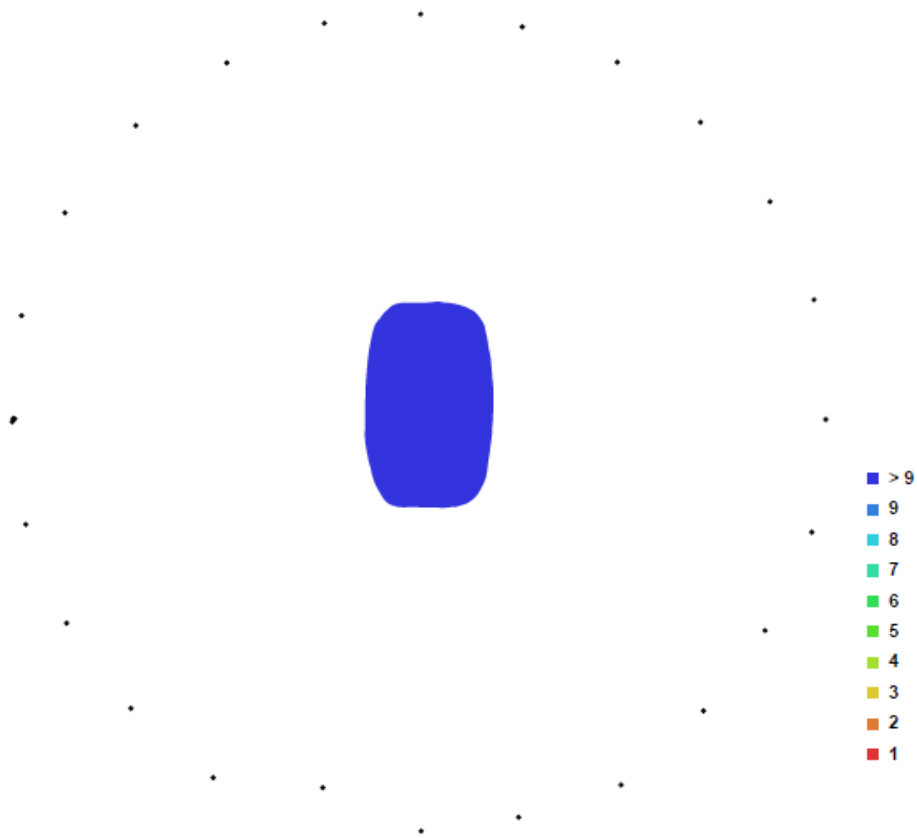


Fig. 1. Camera locations and image overlap.

| | | | |
|--------------------|--------------------|------------------|-------------|
| Number of images: | 26 | Camera stations: | 26 |
| Flying altitude: | 0.725426 m | Tie-points: | 4145 |
| Ground resolution: | 4.85707e-005 m/pix | Projections: | 9724 |
| Coverage area: | 5.10328e-008 sq km | Error: | 1.37935 pix |

| Camera Model | Resolution | Focal Length | Pixel Size | Precalibrated |
|---------------------|-------------|--------------|----------------------|---------------|
| NIKON D3200 (50 mm) | 6016 x 4000 | 50 mm | 3.85319 x 3.85319 um | Yes |

Table. 1. Cameras.

Camera Locations

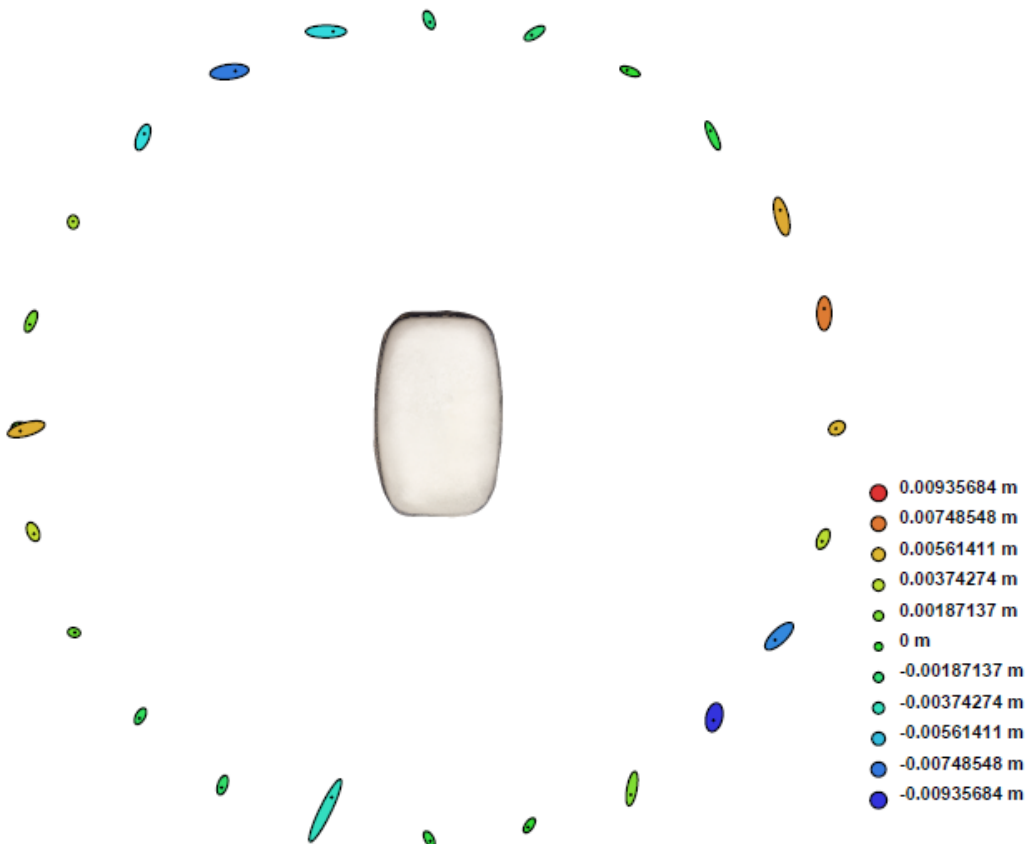


Fig. 3. Camera locations and error estimates.
 Z error is represented by ellipse color. X,Y errors are represented by ellipse shape.
 Estimated camera locations are marked with a black dot.

| X error (m) | Y error (m) | Z error (m) | Total error (m) |
|-------------|-------------|-------------|-----------------|
| 0.008597 | 0.011187 | 0.004334 | 0.014759 |

Table. 2. Average camera location error.

Digital Elevation Model

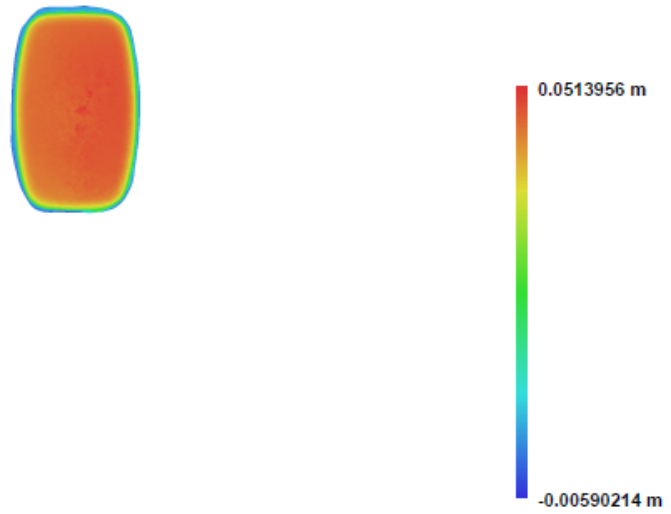


Fig. 4. Reconstructed digital elevation model.

Resolution: 0.000194283 m/pix
Point density: 2.6493e+007 points per sq m

Agisoft PhotoScan

Processing Report
24 April 2015



Survey Data

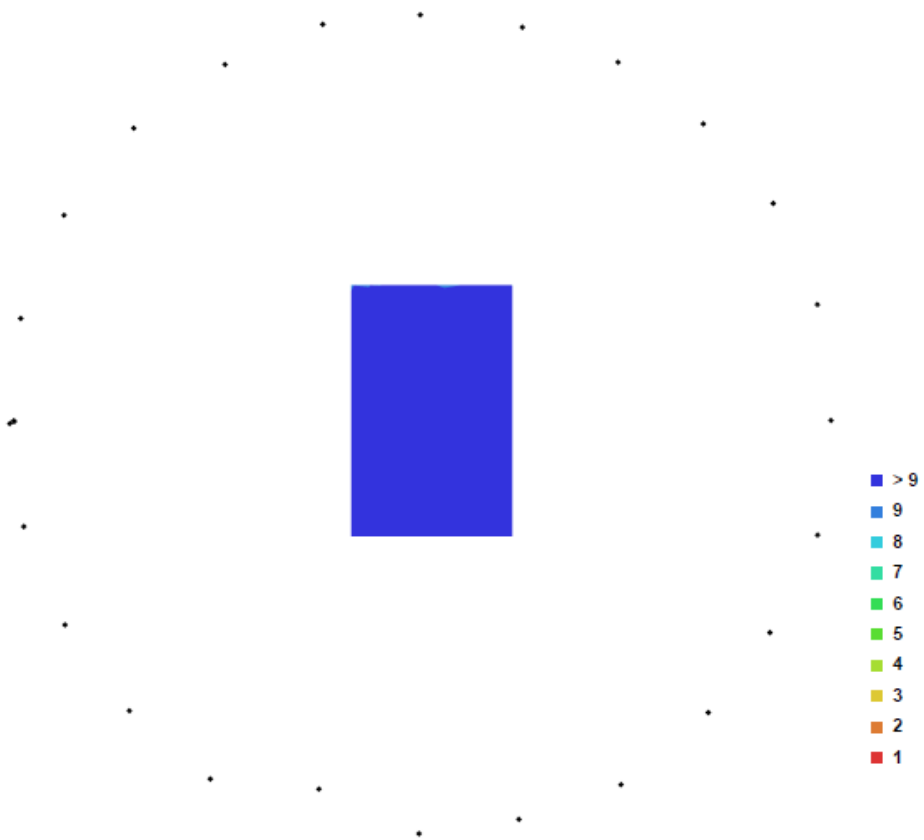


Fig. 1. Camera locations and image overlap.

| | | | |
|--------------------|--------------------|------------------|-------------|
| Number of images: | 26 | Camera stations: | 26 |
| Flying altitude: | 0.718786 m | Tie-points: | 6841 |
| Ground resolution: | 5.06963e-005 m/pix | Projections: | 23253 |
| Coverage area: | 8.67676e-008 sq km | Error: | 1.21482 pix |

| Camera Model | Resolution | Focal Length | Pixel Size | Precalibrated |
|---------------------|-------------|--------------|----------------------|---------------|
| NIKON D3200 (50 mm) | 6016 x 4000 | 50 mm | 3.85319 x 3.85319 um | Yes |

Table. 1. Cameras.

Camera Calibration

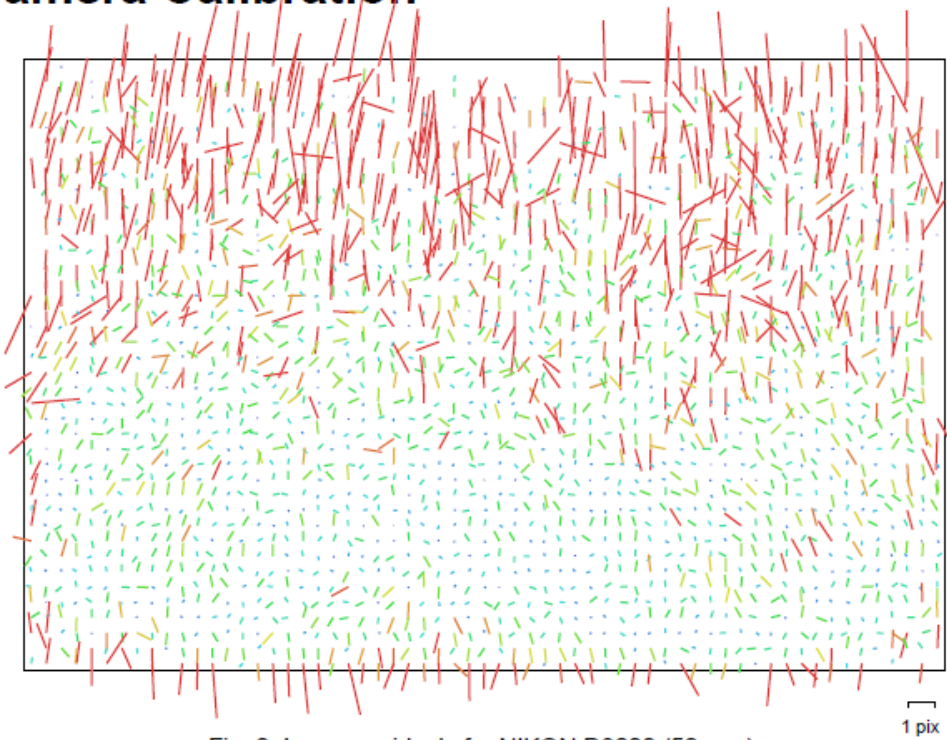


Fig. 2. Image residuals for NIKON D3200 (50 mm).

NIKON D3200 (50 mm)

| | | | |
|-------|---------|-----|-------------|
| Type: | Frame | K1: | -0.248843 |
| Fx: | 14437.8 | K2: | 2.59915 |
| Fy: | 14439.9 | K3: | -20.9077 |
| Cx: | 2891.24 | K4: | 0 |
| Cy: | 1708.8 | P1: | 0.000346748 |
| Skew: | 1.42358 | P2: | -0.00136765 |

Camera Locations



Fig. 3. Camera locations and error estimates.

Z error is represented by ellipse color. X,Y errors are represented by ellipse shape.
Estimated camera locations are marked with a black dot.

| X error (m) | Y error (m) | Z error (m) | Total error (m) |
|-------------|-------------|-------------|-----------------|
| 0.007930 | 0.010778 | 0.001787 | 0.013500 |

Table. 2. Average camera location error.

Digital Elevation Model

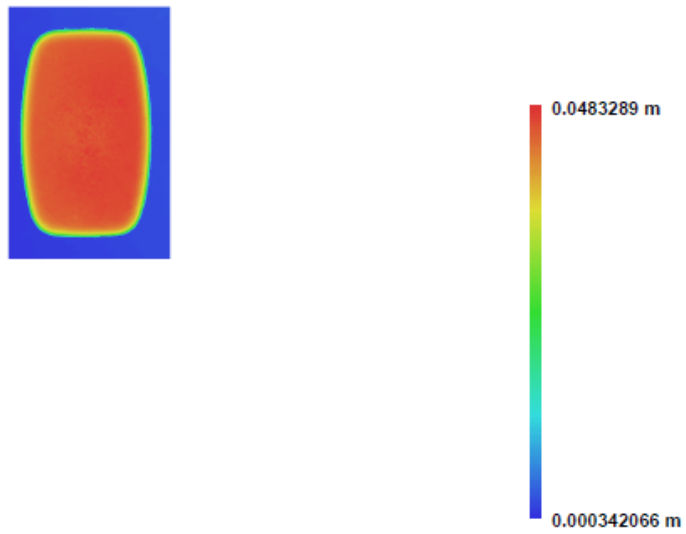


Fig. 4. Reconstructed digital elevation model.

Resolution: 0.000202785 m/pix
Point density: 2.4318e+007 points per sq m

Agisoft PhotoScan

Processing Report
24 April 2015



Survey Data

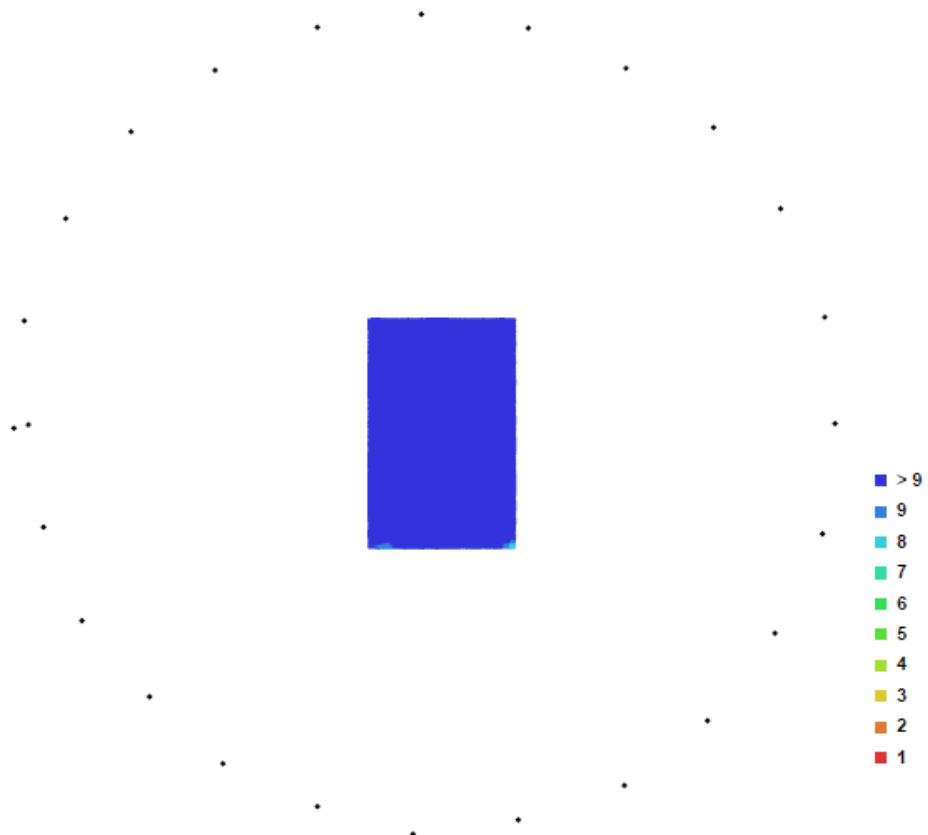


Fig. 1. Camera locations and image overlap.

| | | | |
|--------------------|--------------------|------------------|-------------|
| Number of images: | 25 | Camera stations: | 25 |
| Flying altitude: | 0.708449 m | Tie-points: | 6653 |
| Ground resolution: | 5.09111e-005 m/pix | Projections: | 23137 |
| Coverage area: | 6.95077e-008 sq km | Error: | 1.02526 pix |

| Camera Model | Resolution | Focal Length | Pixel Size | Precalibrated |
|---------------------|-------------|--------------|----------------------|---------------|
| NIKON D3200 (50 mm) | 6016 x 4000 | 50 mm | 3.85319 x 3.85319 um | Yes |

Table. 1. Cameras.

Camera Calibration

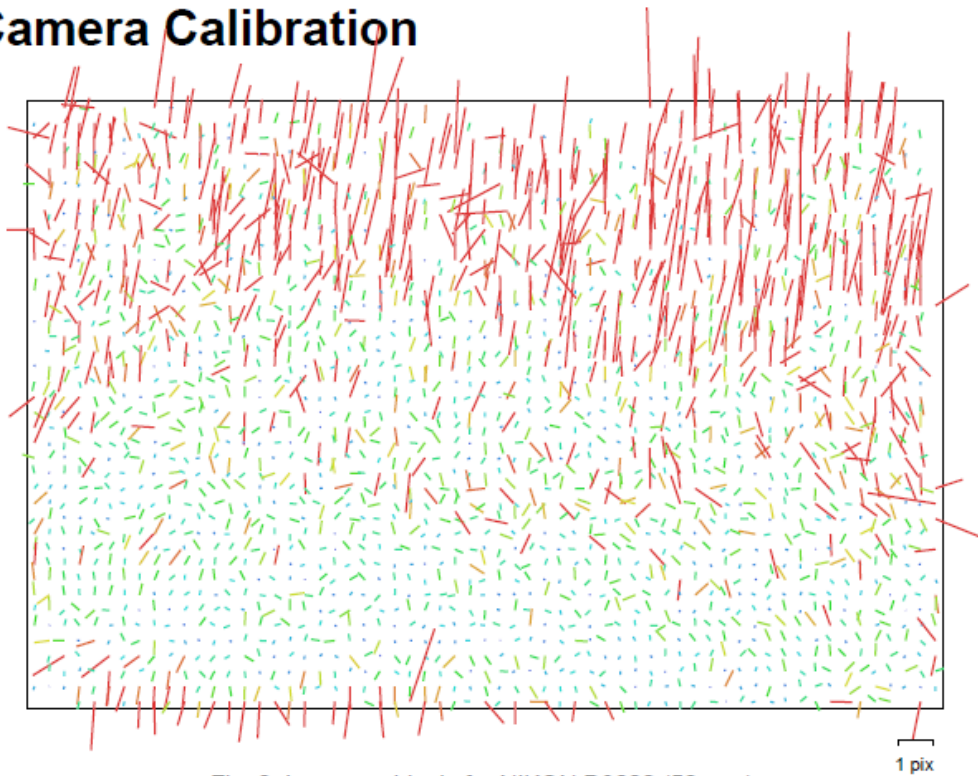


Fig. 2. Image residuals for NIKON D3200 (50 mm).

NIKON D3200 (50 mm)

| | | | |
|-------|---------|-----|--------------|
| Type: | Frame | K1: | -0.139995 |
| Fx: | 14221.8 | K2: | 0.333792 |
| Fy: | 14185.3 | K3: | -1.78282 |
| Cx: | 2991.38 | K4: | 0 |
| Cy: | 1695.79 | P1: | -0.0023196 |
| Skew: | 17.4379 | P2: | -0.000884967 |

Camera Locations

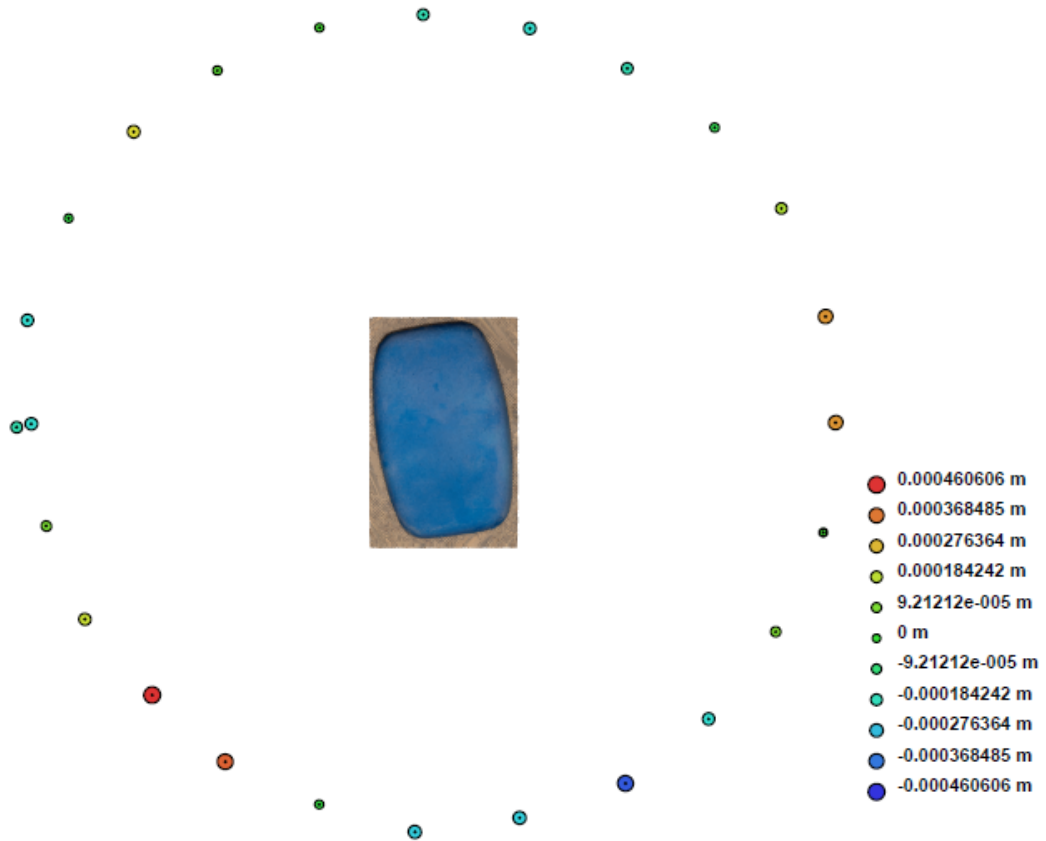


Fig. 3. Camera locations and error estimates.

Z error is represented by ellipse color. X,Y errors are represented by ellipse shape.
 Estimated camera locations are marked with a black dot.

| X error (m) | Y error (m) | Z error (m) | Total error (m) |
|-------------|-------------|-------------|-----------------|
| 0.000207 | 0.000113 | 0.000228 | 0.000328 |

Table. 2. Average camera location error.

Digital Elevation Model

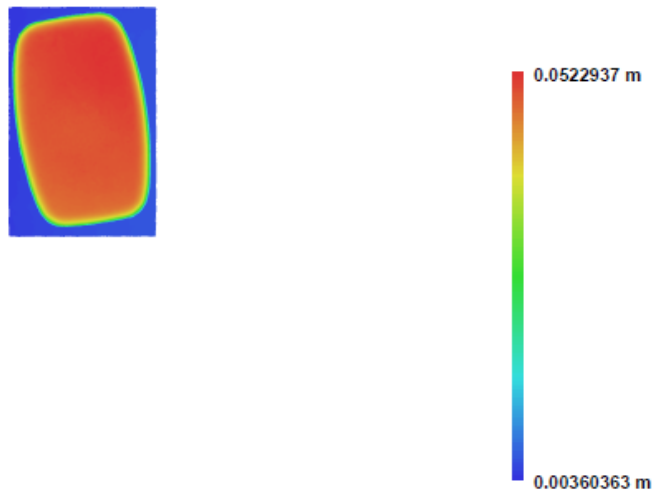


Fig. 4. Reconstructed digital elevation model.

Resolution: 0.000203644 m/pix
Point density: 2.41132e+007 points per sq m